3-11-2011

KAM Torus Frequency Generation from Two-Line Element Sets

Gregory R. Frey

KAM Torus Frequency Generation from
Two-Line Element Sets

THESIS

Gregory R. Frey, Captain, USAF

AFIT/GA/ENY/11-M04

DEPARTMENT OF THE AIR FORCE
AIR UNIVERSITY

AIR FORCE INSTITUTE OF TECHNOLOGY

Wright-Patterson Air Force Base, Ohio

AFIT/GA/ENY/11-M04

KAM Torus Frequency Generation from Two-Line Element Sets

THESIS

Presented to the Faculty

Department of Aeronautics and Astronautics

Graduate School of Engineering and Management

Air Force Institute of Technology

Air University

Air Education and Training Command

In Partial Fulfillment of the Requirements for the

Degree of Master of Science in Astronautical Engineering

Gregory R. Frey

Captain, USAF

March 2011

KAM TORUS FREQUENCY GENERATION FROM TWO-LINE ELEMENT SETS

Gregory R. Frey
Captain, USAF
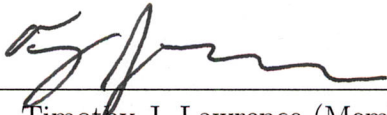
Approved:
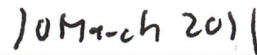
_____   _____
Dr. William E. Wiesel (Chairman)   Date
10 March 2011
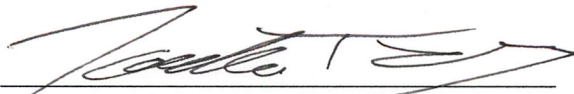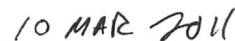
_____   _____
Col. Timothy J. Lawrence (Member)   Date
10 March 2011

_____   _____
Dr. Jonathan T. Black (Member)   Date
10 MAR 2011

AFIT/GA/ENY/11-M04

Abstract

The Kolmogorov Arnold and Moser (KAM) theorem states that a lightly per-turbed Hamiltonian system will have solutions which lie on a torus. The trajectories of Earth orbiting satellites have been shown to lie on KAM tori with three basis frequencies. These basis frequencies are determined by fitting second order polynomials to data from Two-Line Element sets (TLEs) using a least squares technique. The first order coefficients are used as the torus basis frequencies while the second order terms are used to account for perturbations to the satellite's orbit such as air drag. Four cases are attempted using the Hubble Space Telescope and three rocket bodies as test subjects. A KAM torus with the desired basis frequencies is constructed and used to predict satellite position. This position prediction is compared to the position obtained from TLEs using Simplified General Perturbations 4 (SGP4) algorithms. Analysis of the torus position error shows that the torus construction algorithm does not fully characterize the contribution of the smaller basis frequencies to the orbital trajectory.

Acknowledgements

I would like to thank my beautiful wife and my son for all of their love and support as I have gone through this process. Going home each day to them let me relax and keep focused on the bigger picture. Also thanks to a certain 2Lt for developing a great LaTex template which made writing this paper that much easier. Finally, I would like to thank my advisor for all of his support and guidance. His knowledge of orbital dynamics and KAM tori is incredible and was of immeasurable help throughout this entire project.

Gregory R. Frey

Table of Contents

List of Figures

KAM Torus Frequency Generation from Two-Line Element Sets

I. Introduction

1.1 Motivation

Since the launch of Sputnik by the Soviet Union in 1957, there has been a steady increase in the importance of space-based assets to everyday life. Today, everything from banking to car navigation to watching sports on television is either directly tied to, or influenced by capability provided by satellites. The increasing importance of Space has not been limited to the civilian world. In the past decades, the U.S. military has come to increasingly rely on capabilities provided by space assets in everyday operations. These assets provide vital services such as communications, imagery and signals intelligence, and global positioning data to U.S. Military personnel and our allies around the world.

In order to communicate with these on-orbit assets, fixed ground sites and mobile users must know where a satellite will be at a given point in time. Because of this requirement, it is vital that we have an accurate picture of where all space objects are located at the current time, and the capability to rapidly and accurately predict where they will be in the future. In addition to our own satellites, the near-earth environment is filled with thousands of operational commercial and foreign owned satellites as well as many more thousands of pieces of space junk including dead satellites, spent rocket bodies, debris from orbital collisions and trash from past manned space missions. These objects present a hazard to operational satellites, especially when their precise positions are unknown.

The Air Force's current method of orbit propagation uses the Simplified-General Perturbations 4 (SGP4) model which dates back to the 1970s. This model has been adequate but can only accurately predict a satellite's position for a few

days before an update is necessary. If more accurate predictions are needed, for collision avoidance for example, numerical integration is used. While advances in computational technology have greatly reduced the time necessary to perform these integrations, they still take hours to complete. In addition, to predict position one week in advance, the orbit must be integrated through all the intermediate time steps to produce the one needed predicted location. A new method with greater accuracy and less computational and observational cost would be beneficial.

1.2   Approach

This effort will study the feasibility of converting the current method of orbit propagation using SGP4 to one involving a KAM torus. Many of the methods used in the construction of the tori are based on those developed and demonstrated in the past by Wiesel and his past students. This approach may provide increased orbital prediction accuracy at a significantly lower computational and observational cost.

1.3   Problem Statement

This work will answer the question of whether distinct basis frequencies can be extracted from Two-Line-Element-Set (TLE) data, whether KAM tori with those basis frequencies can be constructed from initial position and velocity obtained from TLEs and SGP4, and whether these tori can accurately predict future positions of an Earth orbiting satellite at a level of accuracy equal or greater than that of SGP4.

1.4   Results

KAM torus frequencies were identified for two of four test cases showing that, for certain satellite types in certain orbits, it is possible to extract frequencies from purely observational data. In the two unsuccessful cases, it is believed that a combination of variations in air drag along with inaccuracies in the TLE data were the cause of the poor curve-fits to TLE data. KAM torus construction was attempted

2

for the remaining two test cases. Of these, the construction process was unsuccessful for one case, most likely due to the very small eccentricity of the orbit. In the final case, a KAM torus was constructed and its predicted position was compared to the position predicted at each TLE epoch using SGP4 algorithms. This position comparison showed promising results in that the position error of the torus prediction showed very little linear growth. The error did, however, show significant periodic oscillation. These oscillations were shown to occur at the two smallest torus basis frequencies. It is believed that this is caused by an error in the torus construction process, namely the calculation of Fourier coefficients.

II. Background

2.1 Space Surveillance Network

The Space Surveillance Network (SSN) is a network of 29 sites located around the world. These sites detect and track man-made objects orbiting the Earth including operational and non-operational satellites, spent rocket bodies, debris, and fragments [28]. The SSN operates a variety of sensors to accomplish its mission including phased-array and conventional radars, electro-optical sensors, the Mid course Space Experiment (MSX)- a Low Earth Orbit (LEO) satellite with a payload of sensors spanning UV to very-long-wave IR - and ground-based electro-optical deep space surveillance sites which provide tracking of deep space objects, including geostationary satellites, orbiting above 22,500 miles. Combined, these sensors are responsible for 300,000 to 400,000 observations each day [28]. Figure 1 shows how these sensors are spread over the Earth to provide maximum coverage.
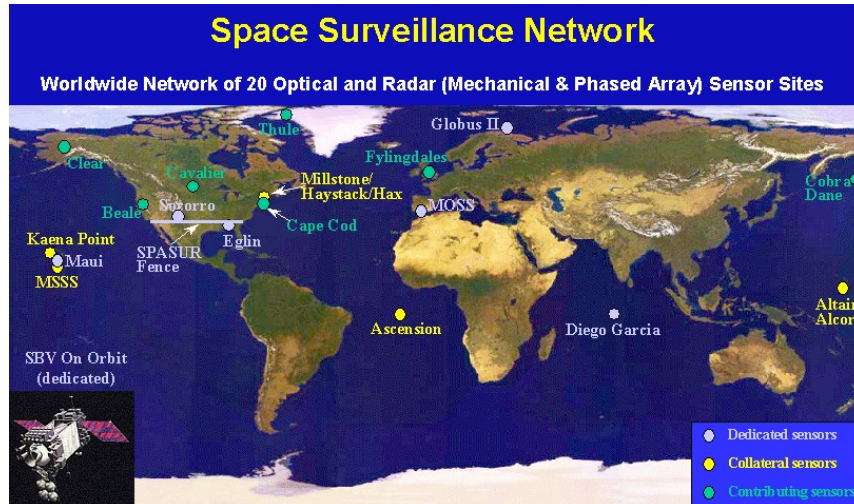
Figure 1: SSN Sites [27]

The SSN monitors space objects using a predictive technique rather than a continuous approach. This means because of the number of objects being tracked and the limited capability of instruments, objects are not tracked in real time. Rather, their position is acquired only periodically. This position is then propagated forward in time using the SGP4 dynamics model. At some later time, SSN instruments

4

then look for the object at the position it was predicted to be and records its actual position, which is hopefully close to the prediction. If a satellite has made an unexpected maneuver during the time between observations, or if the object has experienced greater than expected perturbing forces such as more air drag due to a change in the Earth's outer atmosphere, the process of re-acquiring the object can become time-consuming. A more detailed explanation of orbit determination, and of SGP4, can be found in Section 2.5.

2.2 Orbital Debris

Since the beginning of the space age, the number of objects in orbit has steadily increased to the current number of over 15,000 objects 10cm in diameter or greater being tracked by the SSN. Figure 2 provides a snapshot of the growth of near-earth objects being tracked by the SSN. The large jumps in total number of tracked objects (in 2007 and 2009 for example) are results of satellites breaking up due to explosions or collisions, both intentional and unintentional.
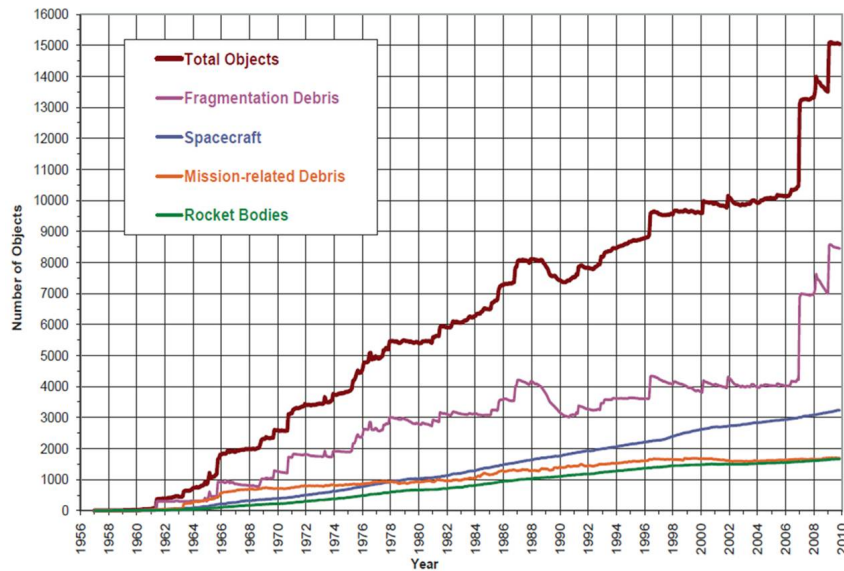
Figure 2: Plot of the Amount of Debris >10cm in Diameter Being Tracked by the SSN [23]

5

Table 1 shows the top 10 such break-ups, in terms of debris created. Approximately one third of all objects currently being tracked are a result of these break-ups. These collisions and explosions result in debris trains that can rapidly circle the earth, endangering any near-by satellites and effectively prohibiting any operational satellite from occupying or crossing that orbital plane. This is demonstrated by Figure 3 which shows the debris train as of December 2007 created by the January 2007 Chinese Anti-Satellite (ASAT) test which destroyed the FENGYUN 1C polar-orbiting weather satellite.

Table 1: Top 10 Breakups as of May 2010 [24]

Common Name	Year of Breakup	Altitude of Breakup (km)	Cataloged Debris	Debris in Orbit	Cause of Breakup
Fengyun-1C	2007	850	2841	2756	Intentional Collision
Cosmos 2251	2009	790	1267	1215	Accidental Collision
STEP 2 Rocket Body	1996	625	713	63	Accidental Explosion
Iridium 33	2009	790	521	498	Accidental Collision
Cosmos 2421	2008	410	509	18	Unknown
SPOT 1 Rocket Body	1986	805	492	33	Accidental Explosion
OV 2-1/LCS 2 Rocket Body	1965	740	473	36	Accidental Explosion
Nimbus 4 Rocket Body	1970	1075	374	248	Accidental Explosion
TES Rocket Body	2001	670	370	116	Accidental Explosion
CBERS 1 Rocket Body	2000	740	343	189	Accidental Explosion
			Total: 7903	Total: 5172	

The hundreds to thousands of pieces of debris caused by each break-up are completely uncontrolled, and therefore present a significant danger to operational satellites orbiting nearby. As the number of orbital objects increase, the probability of future collisions increases. This phenomenon has been examined by Kessler who
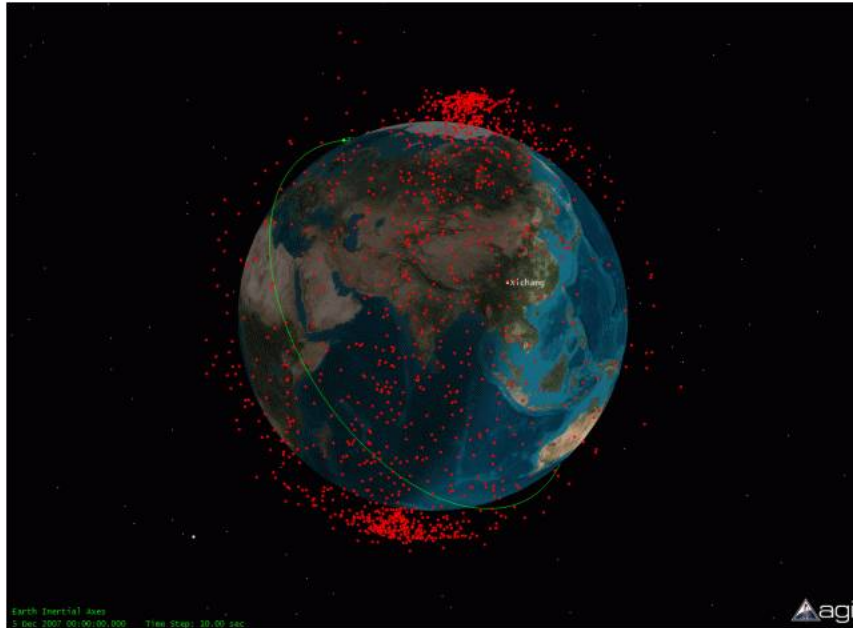
Figure 3: FENYUN 1C Debris (red) from Chinese ASAT Test and ISS Orbit (green) [6]

predicts an increase in collisions and therefore an increase in the amount of debris to a point when the rate of new debris being created exceeds the rate at which objects enter the atmosphere and therefore are eliminated [16]. At that point, entire regions of space could become unusable for operational spacecraft. While many, in fact the majority, of objects in orbit are uncontrolled, those satellites that are most crucial are those that are currently in operation and can therefore, for the most part, be maneuvered. A more accurate method of predicting orbital positions into the future will enhance the ability of these satellites to avoid collisions.

2.3 Collision Avoidance

The importance of precise knowledge of a satellite's position to collision avoidance operations can be seen from the following example. Given a 1km uncertainty in position for two satellites with $1m^2$ cross sections, there is an approximately 1 in 1,000,000 chance that the satellites will actually collide. Therefore, if the satellites were maneuvered each time a collision was possible they would maneuver almost

1,000,000 times to avoid possible collisions before they would maneuver to prevent an actual collision. The vast majority of the time, in other words, the satellites would pass each other with plenty of room to spare even when a collision was predicted. On the other end of the spectrum, the Cosmos-Iridium collision of 2009 demonstrates the fact that predictions of a safe close approach can be unreliable. In that instance, Satellite Orbital Conjunction Reports Assessing Threatening Encounters in Space (SOCRATES) predicted a close approach of 584 m between Iridium 33 and Cosmos 2251 only two hours before they collided [13].

The discussions of Sections 2.1 through 2.3 demonstrate that a more accurate and timely method of orbit determination would be very beneficial - both in the computational and time savings realized in maintaining the orbital catalog and, more importantly, in providing data that could be used to more accurately conduct collision avoidance for U.S. Military satellites. The recent and current research by Wiesel and his students is attempting to determine if a method based on KAM theorem could possibly meet this need.

2.4   Historical U.S. Orbit Determination

The U.S. Government interest in tracking space-objects stems from civilian, scientific, and military needs. The Air Force initially backed efforts to track and catalog space objects in order to have situational awareness in the near-earth environment and therefore have the ability to distinguish between a harmless orbiting satellite and a hostile incoming missile. The first effort to formally track and catalog space objects took place at the National Space Surveillance Control Center (NSSCC) at Hanscom Field in Massachusetts. Satellite observations were taken at more than 150 sites around the world using instruments such as radar, cameras, telescopes, and radio receivers. The observational data was all sent back to the NSSCC where they were first processed manually to calculate corrections to orbital elements before being fed into a computer to produce updated orbital data and ephemeris. The com-

puter output was sent back to the observation sites in the form of bulletins which included data for the next 3-7 days and were used by the sites to plan future observation opportunities. These bulletins were the predecessors to the TLEs currently in use [12].

The U.S. Navy started development on the Naval Space Surveillance System (NAVSPASUR) in 1958. This system consists of a continuous-wave multistatic radar interferometer including 3 transmitters and 6 receivers spread out along a great-circle arc across the country from San Diego, CA to Savannah, GA and is today commonly known as "The Fence". This system is unique in that it detects all objects passing through its sensing area without any prior knowledge of the object's orbit. When The Fence became operational in 1961, a computer required 15 minutes to update a single orbit [12].

The early efforts at orbital tracking by both the Air Force and Navy used a highly simplified dynamics model for orbit determination. In 1959 Brouwer and Kozai published solutions for motion of a satellite under the influence of the Earth's zonal harmonics [3] [17]. These solutions did not include air drag and were consequently modified using various techniques concluding with Lane and Cranford's modification of the Brouwer solution in 1969 [18]. Brouwer's solution was formulated in terms of Delaunay variables and therefore contained the familiar problem of small divisors with eccentricity and inclination. This problem was solved by Lyddane in 1963 who showed the the Brouwer solution could also be expressed in terms of Poincare variables which are the canonical variable counterparts to the equinoctial orbital elements and therefore contain singularities only for retrograde equatorial orbits [21]. Brouwer's solution with Lyddane's modifications was adopted by NAVSPASUR in 1964 and became known as the Position and Partials as functions of Time (PPT) model. The PPT model included an approximation of air drag modeled as influencing the mean motion as a quadratic function of time. In 1997, effects from

the sun and moon were added to the PPT model for high-altitude satellites and the model became known as PPT3 which is currently in use [12].

The Air Force also adopted a model based on the work of Brouwer and Kozai starting in 1960. This model used an air drag model similar to PPT, but instead of using Lyddane's method to avoid the small divisors problem, periodic terms containing eccentricity were neglected. This model became known as the Simplified General Perturbations (SGP) model and became operational in 1964. By 1969, the number of satellites had increased to the point of straining the ability of current-day computers to handle the numerous terms in the SGP model. This led to the empirical atmospheric density model being replaced with an analytic one and SGP being re-worked based on Lane and Cranford's work culminating in a new model, SGP4, becoming fully operational in 1979 [12].

2.5 Current Orbit Prediction and TLE Generation

The SGP4 model is used in conjunction with TLEs. A TLE is, as the name implies, two lines of data providing information such as object identification, time of observation, and orbital elements. Figure 4 shows an example of a single TLE from the Hubble Space Telescope (HST) along with a description of each element.
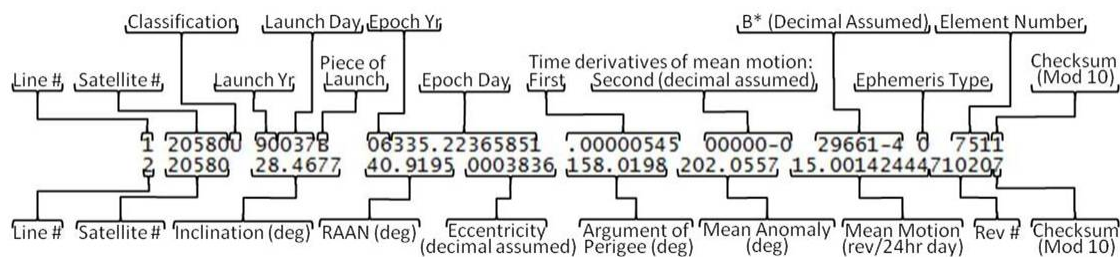
Figure 4: Example TLE for the HST

TLEs for space objects in Low-Earth Orbit (LEO) are generated following initial orbit determination from observations taken by SSN instruments. SGP4 is used for objects with periods less than 225 minutes, while objects with orbital periods

greater than 225 minutes use the Simplified Deep Space Perturbations 4 (SDP4) dynamics model which includes additional effects such as perturbations due to the Sun and Moon. The SGP4 model will be discussed here since all orbits analyzed for this effort are "near-Earth" orbits. As discussed in Section 2.4, the SGP4 model was originally based on a theory of satellite motion perturbed by the Earth's zonal harmonics developed by Brouwer [3]. The model is initialized with the following parameters, all of which are contained within a TLE:

$$
\begin{aligned}
&t_0 && \text{- epoch time} \\
&n_0 && \text{- mean motion at epoch} \\
&e_0 && \text{- eccentricity at epoch} \\
&i_0 && \text{- inclination at epoch} \\
&\omega_0 && \text{- argument of perigee at epoch} \\
&\Omega_0 && \text{- right ascension of the ascending node at epoch} \\
&M_0 && \text{- mean anomaly at epoch} \\
&B^* && \text{- atmospheric drag coefficient}
\end{aligned}
\tag{1}
$$

All of the orbital elements in Equation 1, except the mean motion, are mean orbital elements defined by Brouwer [3]. Brouwer's mean elements are based on the first five terms in the Geopotential (J_1 through J_5) and contain short-period and long-period oscillations. Short period terms contain the mean anomaly in their arguments while long-period terms contain multiples of the mean argument of perigee in their argument. The mean motion follows the convention developed by Kozai and includes only short-period oscillations [17]. Neglecting long period perturbations for mean motion can be a reasonable assumption because, for many earth orbits, long period effects are masked due to the influence of air-drag, which decreases the orbital period and therefore increases the mean motion over long time-scales. Given these initial parameters, the SGP4 model can be used to propagate the orbital elements forward in time by taking into account, again, the Earth's zonal harmonics and also atmo-

spheric drag which is modeled based on a power-law density function. For a detailed description of the SGP4 equations, see Appendix B in [12].

The process of updating a TLE after initial orbit determination starts from a new set of SSN observations, each with an associated time. A typical SSN radar observation contains range, range-rate, azimuth and elevation while an optical observation contains only angular data. These observations then are compared to the predicted observations of the satellite. The predicted values are calculated by propagating the orbit forward in time from the previous TLE using SGP4. Then, the predicted position and velocity of the satellite can be determined at each new observation time and this information can be converted to predicted observation values for the particular sensor which made the actual observation. Having now obtained both predicted and actual observation data, the goal is to minimize the difference between these two sets of values. This is done via a process called differential corrections. Let G be an observation function which expresses the observed values, $\vec{z}$, in terms of the TLE values, $\vec{x}$

$$\vec{z} = G(\vec{x}) \tag{2}$$

What is needed now is a characterization of the effect of changing a TLE value, x_i, on the observation. This could be accomplished by taking a derivative of the observation function, $\frac{dG}{d\vec{x}}$. G, however is complex and not easily differentiable as it takes initial TLE values, propagates them forward using SGP4, and then transforms them to appropriate observation data. Therefore, an approximation of the derivative can be made based on the effect of a small change in $\vec{x}$, $\Delta\vec{x}$:

$$\frac{dG(\vec{x})}{d\vec{x}} \approx \frac{G(\vec{x} + \Delta\vec{x}) - G(\vec{x})}{\Delta\vec{x}} \tag{3}$$

With this approximate derivative, new values of $\vec{x}$ can be calculated that minimize the difference between the predicted and actual observations.

$$\vec{x}_n = \vec{x}_p + [\vec{z}_a - G(\vec{x}_p)] \left(\frac{dG(\vec{x})}{d\vec{x}}^{-1} \right) \Bigg|_{\vec{x}=\vec{x}_p} \tag{4}$$

Once a new TLE is calculated, $\vec{x_n}$, the process is repeated replacing the predicted TLE, $\vec{x_p}$ with the new value until the difference between the two reaches some small tolerance. For a more rigorous discussion of differential corrections and initial orbit determination, see Wiesel or Vallado [36] [30]. New TLEs are generally issued if the difference in predicted position between the old and new element sets is greater than 5km [14].

2.6 Accuracy of TLEs and SGP4

The accuracy of a given TLE varies depending on the number of observations used to generate the TLE, the accuracy of each observation, the current space environment, the type of orbit, and other factors. In general however, a given TLE is typically only valid for a few days at the most before it needs to be replaced. Kelso compared the position of GPS satellites derived from TLEs and SGP4 to precision ephemeris data and found the TLE/SGP4 position to be accurate to only approximately 10km over a period of 15 days [15]. The velocity predictions from TLEs and SGP4 are less accurate than the position because velocity calculations rely on the rates of change of the orbital parameters and the SGP4 model uses certain assumptions, such as a truncated geopotential model, to determine these rates of change.

2.7 Earth Gravitational Model 1996

The gravitational model used in this effort to obtain orbital position data through numerical integration is the Earth Gravitational Model 1996 (EGM96) developed by the National Imagery and Mapping Agency (NIMA), NASA, and the Ohio

13

State University. This model was developed using surface gravity data collected by NIMA as well as satellite altimetry and tracking data from over 20 satellites and consists of spherical harmonic coefficients complete to order and degree 360 [10]. Figure 5 shows a visual representation of EGM96 in the form of deviation from the Earth's Geoid (a sphere with radius equal to the mean ocean surface of the earth).
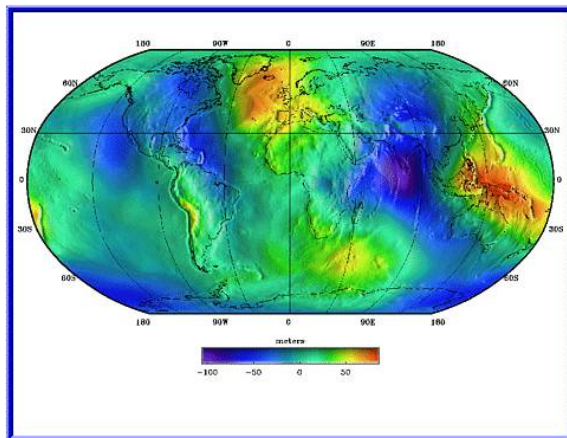
Figure 5: Visual Representation of EGM96 [10]

The EGM96 coefficients are used to construct the expression for the Earth's gravitational potential, V, in spherical coordinates

$$V\left(r, \lambda, \delta\right) = -\frac{\mu}{r} \sum_{n=0}^{\infty} \sum_{m=0}^{\infty} \left(\frac{r}{R_\oplus}\right)^{-n} P_n^m(\cos(\delta)) \left[C_{nm} \cos\left(m\lambda\right) + S_{nm} \sin\left(m\lambda\right)\right] \quad (5)$$

which satisfies Laplace's equation:

$$\nabla^2 V\left(r, \lambda, \delta\right) = 0 \quad (6)$$

where r is the scalar radius, δ is the latitude, and λ is the east longitude. In Equation 5, C_{nm} and S_{nm} are the spherical harmonic coefficients from EGM96 and $P_n^m(\cos(\delta))$ are the associated Legendre polynomials in $\cos(\delta)$. For a derivation of Equation 5 see Wiesel [35]. For this effort, only terms of order and degree less than 20

in the geopotential were used to allow computations to be executed in a reasonable amount of time.

2.8 Hamiltonian Dynamics

Hamiltonian dynamics is a reformulation of classical dynamics first introduced in 1833 by William Hamilton. Hamilton's methods can be used to simplify a complex dynamical problem by writing the equations of motion as first order differential equations. For a given dynamical system, the Lagrangian, L, can be written as a expression of the energy in the system in terms of the system coordinates, their time derivatives, and time

$$L(q_i, \dot{q}_i, t) = T - V \tag{7}$$

where T is the system kinetic energy and V is the system potential energy. L then satisfies Lagrange's equations of motion:

$$\frac{d}{dt}\left(\frac{\partial L}{\partial \dot{q}_i}\right) - \frac{\partial L}{\partial q_i} = 0 \tag{8}$$

which are second order differential equations. The conjugate momenta for the coordinates q_i can the be written as

$$p_i = \frac{\partial L}{\partial \dot{q}_i} \tag{9}$$

A Hamiltonian, $\mathcal{H}$, can then be written for the system

$$\mathcal{H}(q_i, \dot{q}_i, p_i, t) = \sum_i p_i \dot{q}_i - L \tag{10}$$

The velocities, $\dot{q}_i$ can be re-written in terms of q_i, p_i, and t by inverting the expressions for the momenta from Equation 9 and the Hamiltonian can then be written as a function of only the coordinates, momenta, and time:

$$\mathcal{H} = \mathcal{H}(q_i, p_i, t) \tag{11}$$

If the Hamiltonian does not contain time explicitly, it is a constant of the motion. Taking the differentials of Equations 10 and 11 yields:

$$d\mathcal{H} = \dot{q}_i dp_i + p_i d\dot{q}_i - dL(q, \dot{q}_i, t) \tag{12}$$

and

$$d\mathcal{H} = \frac{\partial \mathcal{H}}{\partial q_i} dq_i + \frac{\partial \mathcal{H}}{\partial p_i} dp_i + \frac{\partial \mathcal{H}}{\partial t} dt \tag{13}$$

respectively. Equation 12 can be simplified by expanding dL as

$$dL = \frac{\partial L}{\partial q_i} dq_i + \frac{\partial L}{\partial \dot{q}_i} d\dot{q}_i + \frac{\partial L}{\partial t} dt \tag{14}$$

and re-writing in terms of p_i and $\dot{p}_i$ using Equations 8 and 9

$$dL = \dot{p}_i dq_i + p_i d\dot{q}_i + \frac{\partial L}{\partial t} dt \tag{15}$$

which yields

$$d\mathcal{H} = \dot{q}_i dp_i - \dot{p}_i dq_i - \frac{\partial L}{\partial t} dt \tag{16}$$

Expressions for the time derivatives of the coordinates and momenta can then be written as partial derivatives of $\mathcal{H} = \mathcal{H}(q_i, p_i, t)$ by equating the first two terms of Equations 13 and 16:

$$\dot{q}_i = \frac{\partial \mathcal{H}}{\partial p_i} \ , \ \dot{p}_i = -\frac{\partial \mathcal{H}}{\partial q_i} \tag{17}$$

Equations 17 are a set of first-order differential equations of motion known as Hamilton's equations. A set of q_i and p_i which satisfy Hamilton's equations are said to be *canonical.*

It is evident from Equation 17 that if the Hamiltonian can be written independent of a coordinate q_i or momenta p_i, then the conjugate momenta or coordinate will be a constant. This demonstrates that the correct choice of coordinates and momenta can greatly simplify the dynamics of a system.

2.9 Hamilton-Jacobi Theory

Hamilton-Jacobi Theory builds on the concepts of Hamiltonian dynamics in that it can be used to find the most convenient coordinates and momenta for a system such that they maximize the simplicity of the equations of motion. This is done through the use of a generating function, F, which is a function of a mixture of new and old coordinates and momenta and is used to transform between the new coordinates and momenta, Q_i, and P_i and the old (q_i, p_i). For a discussion on the formulation of generating functions, see Wiesel [35].

Hamilton's equations can be written in the new coordinates and momenta as

$$\dot{Q}_i = \frac{\partial \mathcal{K}}{\partial P_i} \ , \ \dot{P}_i = -\frac{\partial \mathcal{K}}{\partial Q_i} \tag{18}$$

Where $\mathcal{K}$ is the system Hamiltonian expressed in the new coordinates and momenta obtained from the original Hamiltonian and the generating function. The simplest representation of a dynamical system would be when Hamilton's equations are all equal to 0 or, equivalently, when all of the coordinates and momenta are constants. In this case, the new Hamiltonian would be exactly equal to 0 for all time:

$$\mathcal{K} = \mathcal{H}(q_i, p_i, t) + \frac{\partial F}{\partial t} = 0 \tag{19}$$

Where F is the generating function. If an F_2 generating function is used (one written in terms of the old coordinates, the new constant momenta and time: $F_2(q_i, P_i, t)$) the old momenta, p_i can be written in terms of partial derivatives of F_2:

$$p_i = \frac{\partial F_2}{\partial q_i} \tag{20}$$

and Equation 19 can be re-written as a partial differential equation in terms of the generating function, here denoted S

$$\mathcal{H}\left(q_i, \frac{\partial S}{\partial q_i}, t\right) + \frac{\partial S}{\partial t} = 0 \tag{21}$$

The solution to Equation 21 gives the specific generating function S which can be used to transform a system to new coordinates and momenta which are all constant. This generating function is known as Hamilton's Principal Function.

In the special case that the Hamiltonian is independent of time, and therefore a constant of the motion, Hamilton's Principal Function can be separated into two parts: One a function of only the old coordinates and new momenta and one a function only of time

$$S = W(q_i, P_i) + S_t(t) \tag{22}$$

Where W is known as Hamilton's characteristic function. Using this formulation of S, Equation 21 can be written as

$$\mathcal{H}\left(q_i, \frac{\partial W}{\partial q_i}\right) + \frac{\partial S_t}{\partial t} = 0 \tag{23}$$

which can be separated to give

$$\mathcal{H}\left(q_i, \frac{\partial W}{\partial q_i}\right) = P_1 \tag{24}$$

If Hamilton's characteristic function is used as a type 2 generating function, the transformation equations between the new and old coordinates can be written as

$$p_i = \frac{\partial W}{\partial q_i} \ , \ Q_i = \frac{\partial W}{\partial P_i} \tag{25}$$

where the new momenta, P_i, are all constant [35].

The new Hamiltonian can again be written from Equation 19, but since the generating function, W, is independent of time, the new Hamiltonian is equal to the old Hamiltonian, and since the new momenta are all constant, the Hamiltonian must not include the new coordinates. That is

$$\mathcal{K} = \mathcal{H}(P_i) \tag{26}$$

This formulation then results in a system in which the new momenta are all constant while the new coordinates are all cyclic. This can be seen from Hamilton's equations

$$\dot{Q}_i = \frac{\partial \mathcal{K}}{\partial P_i} = \nu_i \,, \; \dot{P}_i = -\frac{\partial \mathcal{K}}{\partial Q_i} = 0 \tag{27}$$

where ν_i are constants.

2.10 Action-Angle Variables

In the case above where the new coordinates are cyclic and the motion of the system is periodic, it is possible to choose another set of coordinates and momenta from which the frequencies of the motion are easily seen. In this case, it is desired that the coordinates be those quantities which are periodic and the conjugate momenta be their associated momenta. A set of coordinates and momenta of this type are known as *Action-Angle variables*. The momenta, or the action variables J, can be calculated from the old coordinates and momenta using the principle of least action [11].

$$J = \oint p \, dq \tag{28}$$

Where the integration is carried out over a complete period of the motion. The conjugate coordinates, or angles w, can then be calculated by first writing Hamilton's characteristic function

$$W = W(q, J) \tag{29}$$

19

and using Equation 25 to find

$$w = \frac{\partial W}{\partial J} \tag{30}$$

The choice of w and J as system coordinates and momenta is beneficial because it can be shown that the time rates of change of the coordinates, $\dot{w}$, are exactly the frequencies associated with the periodic motion of the system [11].

2.11   KAM Theorem

Kolmogorov, Arnol'd, and Moser Theorem, or KAM Theorem, was originally developed in the 1950s as an attempt to solve a type of problem first come upon in the field of celestial mechanics in the 1700s [31]. This problem, now known as the three-body problem (3BP), was posed by Newton who had written differential equations describing the interaction of multiple massive bodies under the influence of gravity. This problem was shown to have a closed-form solution if there were only two bodies (the two-body problem, (2BP)) but if a third body was introduced, no closed form solution could be found. If two of the bodies are much less massive than the third, the system can be expressed as the integrable 2BP with a perturbation due to the third body. This problem was then classically 'solved' using series expansions, but convergence was not possible due to the appearance of small divisors caused by resonances in the Hamiltonian dynamics. In 1954, A.N. Kolmogorov suggested two ideas which are central to the KAM technique [31];

1. Linearize the problem about an approximate solution and solve the linearized problem

2. Improve the approximate solution by using the linearized problem solution as the basis of a Newton-Rhapson method argument

These central ideas were built upon by V. Arnol'd [1] and J. Moser in the 1950s and 1960s and came to be known as KAM theorem.

In words, KAM theorem states that for a integrable system in which the momenta and forces are invariant - that is, a Hamiltonian system - subject to small smooth perturbations from conservative forces, many of the solutions for the unperturbed system are also solutions to the perturbed system with small changes [35]. The perturbed system contains one or more action-angle variables such that the Hamiltonian can be written as

$$\mathcal{H}(J, w) = h(J) + \epsilon f(J, w) \tag{31}$$

where J and w are the action-angle variables, h is the unperturbed Hamiltonian, f is the perturbing function and ϵ is the small perturbing parameter. Therefore, for $\epsilon = 0$ in Equation 31, the Hamiltonian reduces to the initial, integrable system. Solutions to the system then can be shown to have the characteristic of returning to their initial position if one angular coordinate is incremented by an integer multiple of some characteristic angular period while the others are held fixed. This type of solution is defined as a torus. The full mathematical description and proof of KAM theorem can be found in [25] for example.

A torus can be thought of geometrically as the product of N circles, where N is then the dimension of the torus. For example, a one-dimensional torus is simply a circle, while a two-dimensional torus is the product of two circles; Think of the surface formed by revolving a smaller circle around the perimeter of a larger circle, or a donut. An N dimensional torus exists in 2N dimensional phase space. Continuing with the product of circles analogy, the 2N dimensions would be the radius of each circle, the *actions, J*, and the angles, *w*, would be the angles between vectors from the center of each circle to the desired location on the circle and some reference line. Note that the actions are all constant. Figures 6 and 7 show pictures of one- and two-dimensional tori and their action-angle variables.
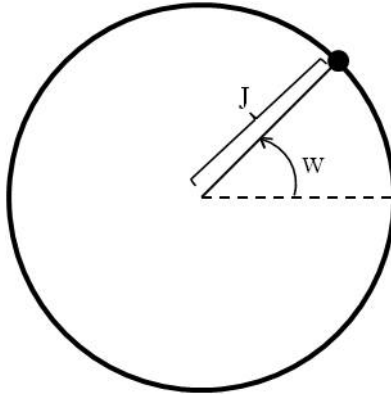
Figure 6: Diagram of a One-Dimensional Torus

Top View

Cut-Away View
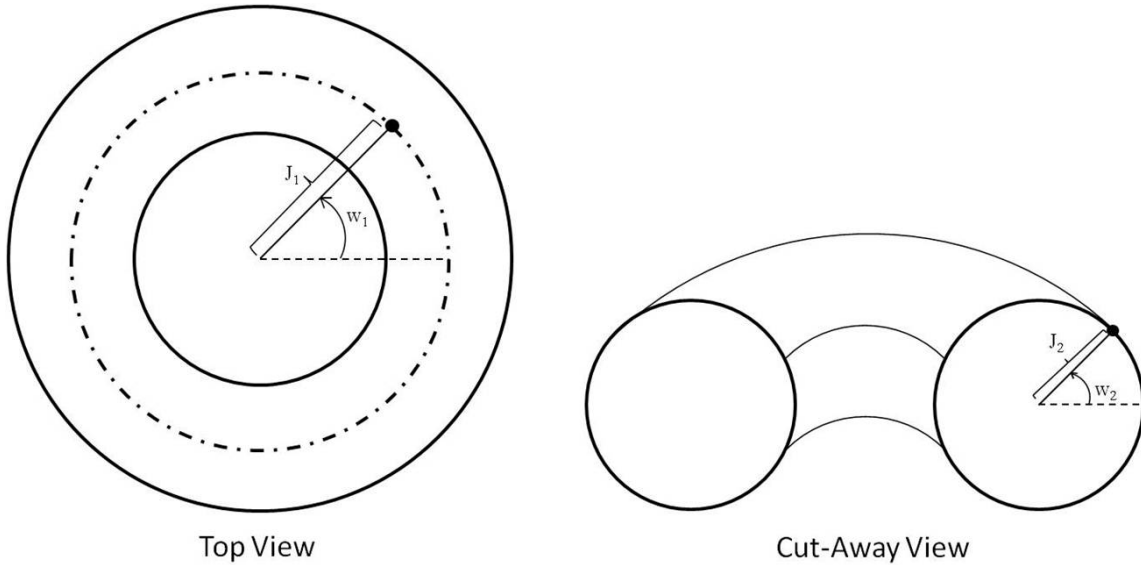
Figure 7: Diagram of a Two-Dimensional Torus

Higher dimensional tori are hard to visualize as they cannot be explicitly drawn in three physical dimensions. However, an example of a three-dimensional torus can be thought of in the following way. Consider a satellite traveling around an orbit with both a precessing argument of perigee and a regressing node. If both ω and Ω are held constant, and the mean anomaly is advanced by $n2\pi$ where n is any integer, the satellite will return to the exact position at which it started. In fact, if *any* two of the three coordinates, (ω, Ω, M) are held fixed while the third is incremented by an integer multiple of 2π, the satellite's position will remain unchanged. Therefore,

the satellite can be said to be traversing a 3-dimensional torus in 6-dimensional phase space, with the dimensions being the three angular coordinates, and the three conjugate action momenta obtained from the system Hamiltonian and Hamilton's equations.

2.12 Reference Frames

The discussions of Sections 2.8 through 2.11 can be applied to the equations of motion for an Earth-orbiting satellite. There are several coordinate frames that can be useful in describing the motion of an Earth-orbiting satellite. Three frames that will be used in this work are the Perifocal (PF) Frame, the Earth-Centered Inertial (ECI) frame, and the Earth-Centered-Earth-Fixed (ECEF) frame. These frames are defined in Table 2.

Table 2: Coordinate Frame Definitions

Coordinate frame	Type	Origin	1-axis	3-axis	2-axis
PF	Inertial	Earth CoM	Toward perigee	Along angular momentum vector	Completes right-handed frame
ECI	Inertial	Earth CoM	Toward vernal equinox	Earth's axis of rotation	Completes right-handed frame
ECEF	Non-inertial	Earth CoM	Toward prime meridian in equatorial plane	Earth's axis of rotation	Completes right-handed frame

2.13 Earth Satellite Dynamics

Let the position of a satellite be denoted in rectangular coordinates in the ECEF frame as x, y, z. The inertial velocity, resolved along the ECEF axes can then be written as

$$\vec{v} = \begin{bmatrix} \dot{x} - \omega_\oplus y \\ \dot{y} + \omega_\oplus x \\ \dot{z} \end{bmatrix} \tag{32}$$

23

Where $\omega_\oplus$ is the rotational rate of the Earth [33]. The kinetic energy, per unit mass of the satellite, can be written as

$$T = \frac{1}{2}\vec{v} \cdot \vec{v} = \frac{1}{2}[(\dot{x} - \omega_\oplus y)^2 + (\dot{y} + \omega_\oplus x)^2 + \dot{z}^2] \tag{33}$$

and the canonical momenta, again per unit mass, are just the velocity components from Equation 32. The potential energy for the system can be written per unit mass as the Earth's geopoential given in Equation 5. The Hamiltonian can then be written from Equation 10, with the $\dot{q}_i$ being written in terms of the momenta from Equation 32.

$$\mathcal{H} = \frac{1}{2}\left(p_x^2 + p_y^2 + p_z^2\right) + \omega_\oplus\left(yp_x - xp_y\right) + V \tag{34}$$

where V is the Geopotential from Equation 5. $\mathcal{H}$ is independent of time and is therefore a constant of the motion. Note that the coordinates in Equation 34 are rectangular while the Geopotential was expressed in spherical coordinates. The transformation between the two sets of coordinates is given by

$$\begin{aligned}
r &= \sqrt{x^2 + y^2 + z^2} \\
\sin\delta &= \frac{z}{\sqrt{x^2 + y^2}} \\
\tan\lambda &= \frac{y}{x}
\end{aligned} \tag{35}$$

where r is the scalar radius, δ is the latitude, and λ is the east longitude.

The motion of an Earth-orbiting satellite is obviously periodic. Wiesel has shown how the basis frequency set of an earth-orbiting satellite can be described by analyzing its position as a function of time as follows [33]. In the Perifocal reference

frame the satellite position can be written as

$$\vec{r}_{pf} = \begin{bmatrix} r\cos(\nu) \\ r\sin(\nu) \\ 0 \end{bmatrix} \tag{36}$$

where r is the scalar orbital radius, and ν is the true anomaly. ν can be written in terms of the mean anomaly, M, and therefore position can be written as a periodic function of the mean anomaly, $\vec{r}_{pf} = \vec{r}_{pf}(M)$. This position can be transformed to the ECEF frame using simple 1 and 3-axis rotation matrices

$$\vec{r}_{ecef} = R_3(-\theta)R_3(-\Omega)R_1(-i)R_3(-\omega)\vec{r}_{pf}(M) \tag{37}$$

Where θ is the Greenwich sidereal time, Ω is the right ascension of the ascending node (RAAN), i is the inclination, and ω is the argument of perigee. θ, Ω, and ω can be written as functions of time as:

$$\begin{aligned} \theta &= \theta_0 + \omega_\oplus t \\ \Omega &= \Omega_0 + \dot{\Omega}t \\ \omega &= \omega_0 + \dot{\omega}t \end{aligned} \tag{38}$$

where the $_0$ subscript denotes value at epoch. Plugging these values into Equation 37 and re-arranging yields

$$\vec{r}_{ecef} = R_3(\theta_0 - \Omega_0)R_3((\omega_\oplus - \dot{\Omega})t)R_1(-i)R_3(-\omega_0)R_3(-\dot{\omega}t)\vec{r}_{pf}(M) \tag{39}$$

From this form, it is apparent that the position vector in the ECEF frame will be dependent on three periodic terms which become the basis frequency set for a KAM torus: $\dot{M}$, $\omega_\oplus - \dot{\Omega}$, and $-\dot{\omega}$. These terms can be written in terms of the other COEs

and the earth's gravitational field, through J2, as

$$
\begin{aligned}
\omega_1 &= \dot{M} = \sqrt{\tfrac{\mu}{a^3}} \left[1 - \tfrac{3J_2 R_\oplus^2}{2a^2(1-e^2)^{1.5}} \left(\tfrac{3}{2} \sin^2(i) - 1 \right) \right] \\
\omega_2 &= \dot{\Omega} - \omega_\oplus = -\tfrac{3\sqrt{\mu}J_2 R_\oplus^2}{2a^{3.5}(1-e^2)^2} \cos(i) - \omega_\oplus \\
\omega_3 &= \dot{\omega} = \tfrac{3\sqrt{\mu}J_2 R_\oplus^2}{2a^{3.5}(1-e^2)^2} \left(\tfrac{5}{2} \sin^2(i) - 1 \right)
\end{aligned}
\tag{40}
$$

Where e is the orbital eccentricity, a is the semi-major axis, μ is the gravitational parameter, and $R_\oplus$ is the radius of the earth. For a derivation of $\dot{M}$, $\dot{\Omega}$, and $\dot{\omega}$, see Danby [8]. Note the ω_2 and ω_3 have switched sign from Equation 39 to Equation 40. This is done to keep the torus frequencies consistent with normal Keplarian mechanics; That is, the line of apsides precesses while the line of nodes regresses.

These frequencies can then be used to form the action-angle variables for the system. Specifically, the *angles* are the linear coordinates with time derivatives equal to the basis frequencies:

$$
\begin{aligned}
Q_1 &= M \\
Q_2 &= \Omega - \omega_\oplus t \\
Q_3 &= \omega
\end{aligned}
\tag{41}
$$

The conjugate action momenta can be calculated from Equation 28 and have been shown to be approximately equal to the Delaunay momenta [34].

$$
\begin{aligned}
P_1 &= \sqrt{\mu a} \\
P_2 &= \sqrt{\mu a}\sqrt{1 - e^2} \cos i \\
P_3 &= \sqrt{\mu a}\sqrt{1 - e^2}
\end{aligned}
\tag{42}
$$

The Hamiltonian, Equation 34, can then be re-written as a function of only the new momenta as

$$
\mathcal{K} = -\frac{\mu^2}{2P_1^2} - \omega_\oplus + \frac{\mu^4 J_2 R_\oplus^2 \left(P_3^2 - 3P_2^2 \right)}{4P_1^3 P_3^5}
\tag{43}
$$

[34]. The action-angle variables in Equations 41 and 42 can then be used to express the motion of an Earth-orbiting satellite as a KAM torus.

2.14   Application to Celestial Mechanics

As noted in Section 2.11, KAM theorem can be applied to lightly perturbed Hamiltonian systems. Since the initial theorem was developed, some effort has been made to apply the theorem to celestial mechanics.

Celletti has done work to apply KAM theorem to a number of celestial mechanics problems including the restricted 3BP, the planetary N-Body problem, and the Spin-Orbit problem in which a rigid, tri-axial satellite orbits a central body and the orbital revolution and rotational motion of the satellite are coupled [4]. In analyzing the specific restricted, circular, planar 3BP of the asteroid 12 Victoria orbiting the Sun and perturbed by Jupiter's gravitational field, Celletti and Chiercha demonstrated an application of an iso-energetic KAM method in which invariant 'trapping' tori are constructed on an energy level similar to the osculating Keplarian motion of the asteroid. These trapping tori then bound the values of the action variables of the asteroid [5].

Robutel demonstrated an application of KAM theorem to the planetary 3BP using canonical heliocentric variables [26]. This choice of variables simplifies the system Hamiltonian and allows the perturbing function to be written in a compact form. The problem is reduced to a four degree of freedom system, resulting in a KAM torus in 4-dimensional phase-space. This torus is shown to be stable for all time for small planetary masses in orbits with small eccentricity and inclination.

McGill and Binney developed method of generating tori for a general gravitational system using a type-2 generating function to map between the action-angle coordinates for a well-known potential and those of the system being investigated [22]. Their method utilizes a non-linear least-squares technique to determine coefficients for the generating function and distorts a 'toy torus' from the well-known system into a torus for the system of interest. They applied their technique to find a torus for Keplarian motion starting from the torus of a degenerate harmonic oscillator.

2.15 Application to Earth-Orbiting Satellites

To date, the only work found related to the application of KAM theorem to Earth-orbiting satellites has been done by Wiesel and his Masters and PhD students.

Wiesel's first article on the subject showed that the KAM theory could best be applied to earth orbiting satellites when their motion was expressed in the Earth-Centered-Earth-Fixed (ECEF) coordinate frame [33]. In this frame, the Earth's gravitational field is nearly constant and the the system momenta can be written simply as the time derivatives of the coordinates, that is, as the velocity components as demonstrated in Section 2.13. The Hamiltonian can then be written independent of time in terms of only the momenta and the gravity field and is therefore an integral of the motion. Using orbital position data obtained from a one-year numerical integration, Wiesel extracted the frequency content of the orbit using a Fast Fourier Transform (FFT) and showed that for nearly circular orbits with moderate inclination, the frequency spectrum exhibited clearly defined peaks which were linear combinations of only three discrete basis frequencies, showing that their motion might lie on a KAM torus. For orbits with inclinations near 90 degrees, the frequency spectra were not as clean, exhibiting nearly chaotic behavior. In order to more precisely define the basis frequencies, a method was used based on the work of Laskar [19]. Having obtained the basis frequency set, the orbital data was fit to a Fourier series in the basis frequencies. This Fourier series contains the torus coordinates and is used to transform from torus coordinates to physical cartesian coordinates. A version of this process was used for the current effort and will be described in Section 3.5.

In subsequent work, Wiesel further analyzed the frequency spectrum of a earth-orbiting satellite from orbital data obtained using a simplified version of SGP4 [34]. This analysis showed that the most prominent spectral lines occur in clusters around multiples of the anomalistic frequency, $\dot{M}$, separated by combinations of the rotational rate of the Earth, the nodal regression rate and the rate of perigee precession.

Wiesel then compared the trajectories obtained from a KAM torus, constructed by the method described by in [33], with tori obtained using the simplified SGP4 model and the 2BP. The trajectories from these tori were then compared to a numerically integrated trajectory. The KAM torus was accurate to within 30 meters over six months while the SGP4 torus was accurate only to within 40 kilometers.

Derbis analyzed precise orbital data from 26 GPS satellites using a Fast Fourier Transform (FFT) to extract approximate basis frequencies [9]. These frequencies were compared to those obtained from numerically integrated orbital data and the Laskar frequency method. The two methods yielded similar but not exact duplicate frequency sets. Her research also illustrated two difficulties in applying KAM theorem to artificial satellites. If pairs of basis frequencies are near-integer multiples of each other (nearly commensurate), the basis set becomes hard to determine because the spectral lines lie nearly on top of each other. In Derbis' case, this difficulty presented itself in $\omega_2 \approx 2\omega_1$ because the GPS constellation has an orbital period of 12 hours, or one-half the rotational period of Earth. The other difficulty was seen when analyzing data from the oldest GPS satellite which uses only 3 reaction wheels for attitude control and must periodically do momentum dumps. These momentum dumps result in nearly-impulsive $\Delta v's$ which, although small, do not fit the KAM theorem criteria of *small smooth perturbations*. As a result of this, the spectral map of this satellite exhibited significant noise and revealed basis frequencies which differed from the other GPS satellites. This shows that KAM theorem must be applied carefully to operational satellites that maneuver from time-to-time as a large enough maneuver will move the satellite off of the torus. Current research is being done on the behavior of motion near a KAM torus in the hope of determining a way to account for this.

Little analyzed orbital data from the Gravity Recovery and Climate Experience (GRACE) and Jason-1 satellites and determined their basis frequencies using the Laskar method [20]. The predicted position from the resulting torus was then

compared to the actual position data to determine its accuracy. Based on the growth rate of the position error, the basis frequencies were adjusted which resulted in a torus which provided significant improvement in position accuracy. Using this process, KAM torus position data for the Jason-1 satellite was shown to be accurate to about 1 kilometer over 15 days, while the torus for the GRACE satellite was accurate to only approximately 15 kilometers over the same time period. The residual growth in the GRACE data was quadratic which was taken to be a result of air drag. Because air-drag is a non-conservative force, it cannot be readily incorporated into the KAM theorem. This is also a topic of current research.

Craft performed an analysis of the effect of the number of terms in the torus Fourier series to position accuracy, measured against a numerically integrated orbit [7]. He showed that the ideal number of series terms, with respect to accuracy and computational burden, is between 1500 and 2000. For his test cases, this number of terms resulted in an rms error in the position components on the order of 10^{-2}km. Craft also studied the applicability of KAM theorem to satellite formation flight [7]. In this analysis, a torus was constructed for a chief satellite and a deputy satellite was placed on the same torus at an offset of one or more of the torus angle coordinates. This resulted in a position difference between the chief and deputy which was oscillatory in time and contained a small secular drift rate proportional to the initial displacement.

Bordner attempted to fit KAM tori to high-precision orbital data for GPS satellites using a variety of spectral methods based on those developed by Laskar and Wiesel, but was unable to produce a torus with suitable accuracy [2]. He encountered the same difficulties with near-commensurate frequencies as Derbis, and also found ω_3 very hard to identify using spectral methods because its period was very long compared to the timespan of the data being analyzed. Another method of developing the torus Fourier series was attempted, this time using a least squares approach to fit the coefficients of the series after obtaining the basis frequencies. This method

yielded improved accuracy, but still had errors in excess of acceptable levels for the GPS constellation.

Bordner also developed methods for torus construction from numerically integrated trajectories. The most successful method was shown to be one in which clusters of peaks in the frequency power spectrum were decomposed simultaneously. This method allowed ω_3 to be identified more easily as the separation between the dominant peak and its flanking peaks in each cluster. Using this technique, position errors were shown to drop to 10s of meters over a period of 6 months for certain low-earth orbits [2].

2.16 Contribution of Current Work

The current work will build on the results described above in Section 2.15 in a number of ways. First, an attempt will be made to identify KAM torus basis frequencies from purely observational data in the form of TLEs. This is in contrast to the current method of obtaining the basis frequencies from a numerically integrated trajectory. A Matlab script will be developed to read in and format TLE data to enable basis frequency identification through least-squares curve fitting. The script will also read in and format additional TLE data, such as the bstar drag term, which could be used to build on the current effort in future work. This work will also demonstrate a new technique of making small changes to a torus' basis frequencies by first calculating a torus momenta offset corresponding to a known frequency offset and then translating that momenta offset to a change in initial velocity. This frequency matching process can be utilized in an iteration with the current torus construction algorithm to obtain a torus with basis frequencies nearly exactly equal to the desired values. Finally, this work includes a detailed analysis of the frequency content of torus position error data which can be used going forward to refine the torus Fourier series construction algorithms to produce tori with more accurate position prediction capability.

III. Methodology

3.1 Test Object Selection and Data Gathering

The TLEs used for this effort were obtained from the website http://celestrak.com. This site allows the user to request historical TLEs for any object in the satellite catalog. As discussed in Section 2.15, previous research has demonstrated that certain types of orbits cause difficulties in applying KAM theorem to Earth satellites. These difficulties were taken into account in selecting test objects for this effort. Table 3 lists each known issue and describes how each was accounted for in selecting the current test objects.

Table 3: Test Object Selection Criteria

Issue	Object Selection Criteria
Air Drag	Choose objects orbiting above 300km altitude that have been in stable orbits for a long period of time.
Station Keeping	Choose either non-operational objects or operational objects which use only reaction wheels for attitude control.
Near-Commensurate Frequencies	Choose objects such that the Earth's rotational period is not nearly an integer multiple of the orbital period.
Near-Polar Inclination	Choose objects with inclination below critical.

This analysis led to the choices of three spent rocket bodies and the HST as test subjects for this effort. General information on the approximate orbits of each of these satellites is in Table 4.

Table 4: Orbital Information for Test Satellites

Name	Catalog Num.	Launch Date	Period [min]	Inclination [deg]	Apogee altitude [km]	Perigee altitude [km]	Eccentricity
Hubble Space Telescope	20580	4/24/1990	95.93	28.47	566	561	3.836E-4
Thor Ablestar Rocket Body	59	10/4/1960	106.44	28.25	1203	921	1.893E-2
Delta 1 Rocket Body No.1	341	7/10/1962	157.52	44.77	5619	949	2.414E-1
Delta 1 Rocket Body No.2	8133	8/27/1975	95.21	25.30	700	357	2.753E-2

A Matlab script was written to read a text file containing multiple TLEs. This raw data was then converted to units and format useful for further analysis. All angular data in TLEs is reported in degrees, from 0 to 360. These values were converted to radians, and the 2π jumps were eliminated, resulting in smooth plots of RAAN and argument of perigee as functions of time. The mean anomaly data was merged with the revolution number data to form a continuous plot of M vs.

time. Time in TLEs is represented as a number between 0 and 367 which gives the day (and partial day) of the year, starting from 0000 UT 31 Dec. For example, a epoch time of 09001.000000000 corresponds to 0000 UT on 01 Jan 2009, while an epoch time of 09000.00000000 corresponds to an epoch time of 0000 UT on 31 Dec 2008. All times are measured in mean solar days (24 hour days) rather than sidereal days. The Matlab script converted this raw data to a continuous timescale, starting at zero, and changed units from mean solar days, to sidereal days, to canonical time units (TUs) as was necessary.

3.2 TLE Frequency Identification

After the data was read-in and formatted, further analysis was done to extract the characteristic frequencies of the orbit, that is:

$$\frac{\partial M}{\partial t}, \frac{\partial \Omega}{\partial t}, \frac{\partial \omega}{\partial t} \tag{44}$$

To do this, a second order curve-fit was accomplished using a least squares technique as follows:

Let the data to be fit be represented as a vector $\vec{d}$ while the time corresponding to each data point is grouped into a vector $\vec{t}$. Then, the second order curve fit will be of the form

$$\vec{d} = a_0 + a_1\vec{t} + \frac{1}{2}a_2\vec{t}^2 \tag{45}$$

where a_i are the curve-fit coefficients. Next, define a matrix T as

$$T = \frac{\partial \vec{d}}{\partial a_i} = \begin{bmatrix} \vec{1} & \vec{t} & \frac{1}{2}\vec{t}^2 \end{bmatrix} \tag{46}$$

where $\vec{1}$ is a column vector of the same length of $\vec{t}$ containing all ones. Now, the curve-fit coefficients can be solved for

$$\vec{a} = \left(T^T Q^{-1} T\right)^{-1} T^T Q^{-1} \vec{d} \tag{47}$$

where Q is assumed to be the identity matrix for now since the individual data point covariances are not known. The curve fit is then given by

$$\vec{f} = T\vec{a} \tag{48}$$

and residuals, $\vec{r}$, can be calculated:

$$\vec{r} = \vec{d} - \vec{f} \tag{49}$$

To determine the accuracy of the curve-fit, the covariance matrix, $\vec{P}$, was calculated

$$\vec{P} = \left(T^T Q^{-1} T\right)^{-1} \vec{r_0} \tag{50}$$

where $\vec{r_0}$ is the average squared residual, which we take to be approximately equal to the standard deviation squared, σ^2

$$\vec{r_0} = \frac{1}{N} \sum_{i=1}^{N} \vec{r_i^2} \approx \sigma^2 \tag{51}$$

and N is the number of data points.

For the HST for example, these curve fits came out to:

$$M = 1.166155 \times 10^{-5} t^2 + 9.425866 \times 10^1 t + 3.487986$$

$$\Omega = -3.228504 \times 10^{-8} t^2 - 1.137980 \times 10^{-1} t + 7.145640 \times 10^{-1} \tag{52}$$

$$\omega = -4.202363 \times 10^{-8} t^2 + 1.853485 \times 10^{-1} t + 2.714583$$

With time in units of mean solar days. Note that the coefficients have been rounded and more significant digits were carried in the actual calculations. As expected, the second order terms in the curve-fits are much smaller than the lower order terms. These second order terms appear due to the presence of air-drag and other low-order effects. In forming the initial KAM tori, the desired basis frequencies were based on the first order curve-fit coefficients and second order effects were accounted for later.

3.3 Canonical Units

In many of the calculations performed, canonical units of distance units (DUs) and time units (TUs) were used. The values used for these quantities were

$$1 \, DU = 6378.135 \, km$$
$$1 \, TU = 13.44686457 \, min$$

(53)

3.4 Position and Velocity

In order to numerically integrate the trajectory and obtain a data set from which to build a torus, an initial position and velocity is necessary. This was obtained from the TLEs using the SGP4 algorithms developed by Vallado in C++ and subsequently translated to Matlab. This code is available for download on the internet [29]. The SGP4 algorithm outputs position and velocity in the True Equator Mean Equinox (TEME) reference frame, which is nearly the ECI frame. As discussed in Section 2.15, position and velocity data are needed in the ECEF frame. This was accomplished using a modified version of the Matlab routine teme2ecef, also from Vallado, to output position and velocity in the Pseudo Earth-Fixed (PEF) frame which is equivalent to the ECEF frame described in Section 2.12. As an example, Figure 8 shows the position of the Thor Rocket Body at the epoch time of each TLE. While this data does not appear to look like an orbit, it is important to recognize

35

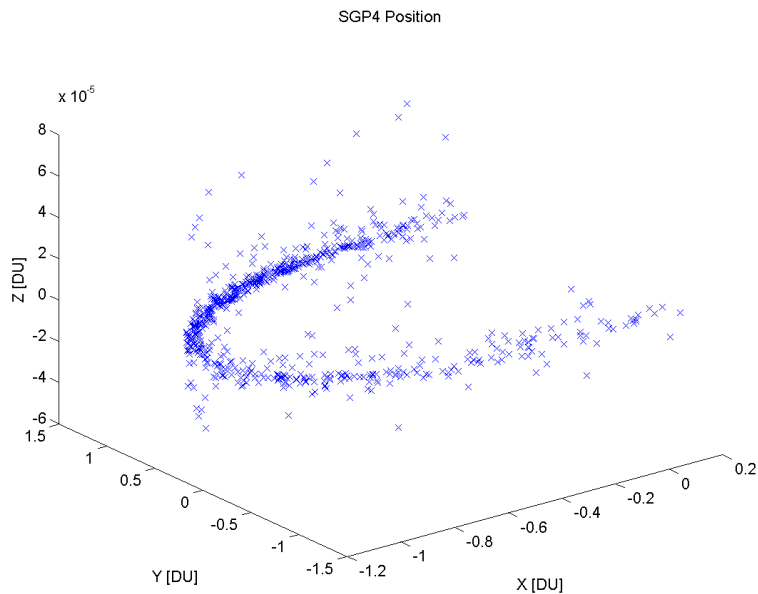that the data points are, on average, about 12 hours apart and therefore do not show the continuous trajectory.

Figure 8: SGP4 Position at each TLE Epoch for Thor Rocket Body

3.5   Torus Construction

3.5.1   Numerical Integration.   The initial position and velocity vectors obtained from the first TLE using SGP4 were input into a numerical integration routine developed by Wiesel which calculates a trajectory taking into account the first 20 terms in the Earth's geopotential from EGM96 described in Section 2.7. The routine is a 4th order predictor-corrector algorithm which runs first backward and then forward in time. Error checking is done by calculating the Hamiltonian given in Equation 34 at each time step and ensuring its value does not change. For the current analysis, the orbits were integrated forward and backward for 6 months, resulting in one year's worth of position data. For all cases, error in the Hamiltonian did not exceed $\mathcal{O}10^{-13}$.

3.5.2 Torus Frequency Identification.   The numerical data was then an-
alyzed to identify the orbit's fundamental frequencies given in Equation 40. To
accomplish this, a modified Laskar frequency algorithm developed by Wiesel was
used [35]. A finite Fourier transform of the form

$$\phi(\omega) = \frac{1}{2T} \int_{-T}^{T} q(t) e^{i} \mathcal{X}_p(t/T) dt \tag{54}$$

was performed on the numerically integrated data where ω is frequency, q is the
physical coordinate (x, y, or z), t is time, T is the total integration time, and $\mathcal{X}_p$ is
a Hann window function given by

$$\mathcal{X}_p(t/T) = \frac{2^p (p!)^2}{(2p)!} \left(1 + cos\left(\frac{\pi t}{T} \right) \right)^p \tag{55}$$

where p is a parameter which, when increased, helps to widen the central peak in
$\phi(\omega)$ while reducing the magnitude of any side lobes. Care must be given when
increasing p however, for if peaks in $\phi(\omega)$ are close together, a value of p which is
too high can cause the larger peak to obscure the smaller one. For this work a value
of $p = 2$ was used.

To identify the basis frequency set, the power spectrum, $P = |\phi|^2$, was com-
puted. Previous research by Wiesel has shown that the power spectra for Earth-
orbiting satellites contain multiple clusters of three peaks centered around integer
multiples of the first basis frequency ($\dot{M}$ or ω_1) [34]. Figure 9 shows the power spec-
trum from the Thor Rocket Body and illustrates the first two of these peak clusters,
which are the largest in magnitude and are centered around ω_1 and $2\omega_1$. The sepa-
ration between the peaks in each cluster is the second basis frequency, ω_2. Note that
the major peaks in the X and Y spectrum are identical while the Z peaks are offset.
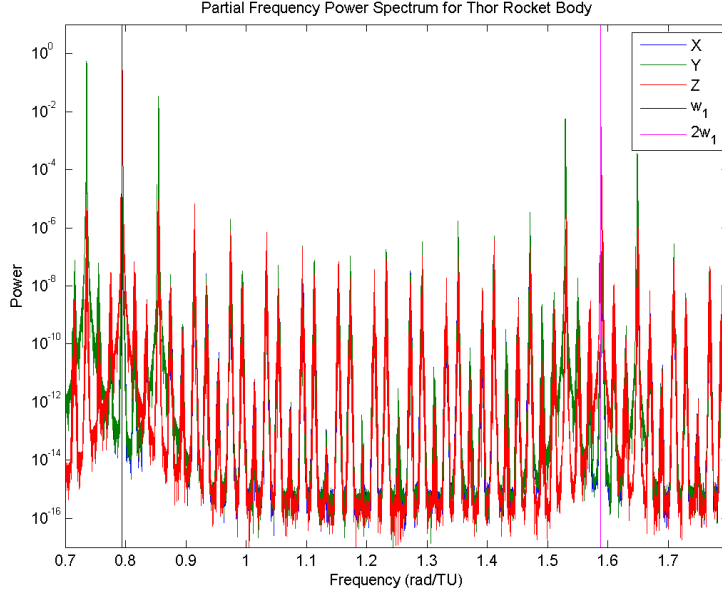
37

Figure 9: Thor Rocket Body Frequency Power Spectrum Illustrating Peak Clusters Around ω_1 and $2\omega_1$

The values of each of these peaks is, as linear combinations of ω_1, ω_2, and ω_3:

$$
\begin{aligned}
x_{1a} &= \begin{bmatrix} 1 & 1 & 1 \end{bmatrix}^T \\
z_1 &= \begin{bmatrix} 1 & 0 & 1 \end{bmatrix}^T \\
x_{1b} &= \begin{bmatrix} 1 & -1 & 1 \end{bmatrix}^T \\
x_{2a} &= \begin{bmatrix} 2 & 1 & 1 \end{bmatrix}^T \\
z_2 &= \begin{bmatrix} 2 & 0 & 1 \end{bmatrix}^T \\
x_{2b} &= \begin{bmatrix} 2 & -1 & 1 \end{bmatrix}^T
\end{aligned}
\tag{56}
$$

Local maxima in the power spectrum are then searched for at these locations using a Newton-Rhapson method, starting from the approximate peak locations calculated from Equation 56 and using the J2 frequencies given in Equation 40. Having found the actual locations of the three peaks with the largest amplitude, a simple linear system can be solved for the actual values of the basis frequencies: ω_1, ω_2, and ω_3.

38

3.5.3 Fourier Series Construction. Having obtained the torus basis frequency set, in order to describe the satellite motion as a KAM torus, the physical coordinates, q_i must be expressed as a Fourier Series in the basis frequency set and torus coordinates. This Fourier series can be written as

$$\vec{q} = \sum_{\vec{j}} \left(\mathcal{C}_{\vec{j}} \cos \vec{j} \cdot \vec{Q} + \mathcal{S}_{\vec{j}} \sin \vec{j} \cdot \vec{Q} \right) \tag{57}$$

where $\vec{j}$ is a vector summation index, each vector entry identifying a spectral peak as, for example, in Equation 56, $\mathcal{C}$ and $\mathcal{S}$ are the yet to be solved for matrices of Fourier coefficients, and $\vec{Q}$ are the torus coordinates which are linear functions of time, with time derivatives equal to the basis frequency set. As noted before, Craft showed that the optimum number of terms in this Fourier series was between 1500 and 2000. Consequently, 1750 terms were included in the current effort.

The Fourier coefficients can be solved for by a number of methods as described in [35]. The method used for this work was the frequency cluster decomposition method studied and demonstrated by Bordner [2]. This method takes advantage of the fact that maxima in the power spectra occur at intervals equal to the second basis frequency, ω_2, as shown previously in Figure 9 and smaller peaks around these are separated by ω_3. This can be seen in Figure 10. Consequently, clusters of peaks can be analyzed to determine their Fourier coefficients simultaneously. This method simplifies the calculations in that it transforms the calculation of Fourier coefficients from solving a single large linear system to simultaneously solving multiple small linear systems which reduces the total amount of calculation required.

3.6 Transition to a Nearby Torus

The torus obtained through a first iteration of the method described in Section 3.5 was a valid KAM torus, however it is not the torus which will describe the motion of the satellite in question because its basis frequencies were not the desired
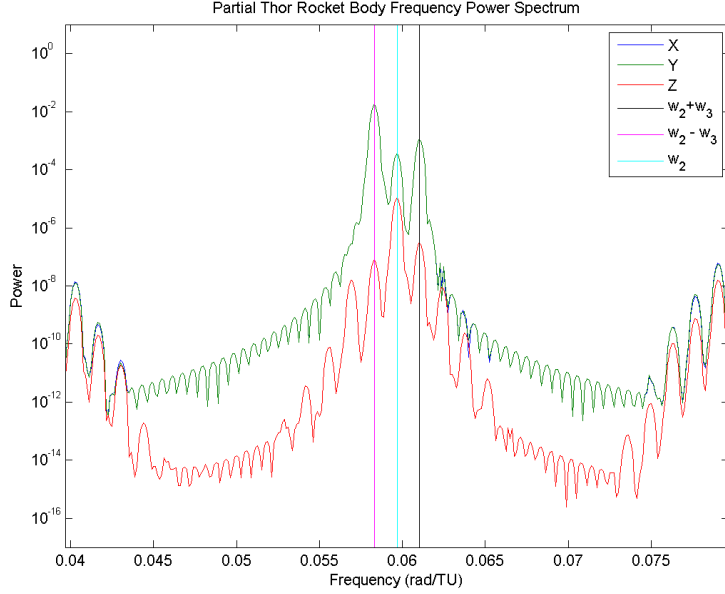
Figure 10: Thor Rocket Body Frequency Power Spectrum Peak Separation by ω_3

frequencies, those obtained via the TLE curve-fits in Section 3.2. This is most likely due to the inherent inaccuracies of SGP4, specifically the velocity. Therefore, the initial velocity was changed in such a way that the method of Section 3.5 yielded a torus with the desired frequencies. This was done using the following process.

The reference (first-iteration) torus basis frequencies are grouped into a vector, $\vec{\omega}$, while the desired torus frequencies from the TLE data are grouped into $\vec{\omega}_0$. Then, the frequency error can be written as

$$\Delta\vec{\omega} = \vec{\omega} - \vec{\omega}_0 = \frac{\partial\vec{\omega}}{\partial\vec{P}}\Delta\vec{P} \tag{58}$$

where $\vec{P}$ is a vector of the reference torus momenta and $\Delta\vec{P}$ is the unknown momentum offset between the reference and desired tori. Equation 58 can be solved for $\Delta\vec{P}$ which yields

$$\Delta\vec{P} = \frac{\partial\vec{\omega}}{\partial\vec{P}}^{-1}\Delta\vec{\omega} \tag{59}$$

The Jacobian matrix $\frac{\partial \vec{\omega}}{\partial \vec{P}}$ can be found analytically using 2BP orbital elements and taking the torus momenta to be the DeLaunay momenta,

$$
\begin{aligned}
P_1 &= \sqrt{\mu a} \\
P_2 &= \sqrt{\mu a}\sqrt{1 - e^2} \cos i \\
P_3 &= \sqrt{\mu a}\sqrt{1 - e^2}
\end{aligned}
\tag{60}
$$

The Hamiltonian can then be written, through J_2, as

$$
\mathcal{K} = -\frac{\mu^2}{2P_1^2} - \omega_\oplus + \frac{\mu^4 J_2 R_\oplus^2 \left(P_3^2 - 3P_2^2\right)}{4P_1^3 P_3^5}
\tag{61}
$$

which is the same expression as Equation 43. The approximate torus frequencies, again through only J_2, can be expressed as partial derivatives of the Hamiltonian

$$
\vec{\omega} = \frac{\partial \mathcal{K}}{\partial \vec{P}}
\tag{62}
$$

and therefore the Jacobian from Equation 59 can be expressed as

$$
\frac{\partial \vec{\omega}}{\partial \vec{P}} = \frac{\partial^2 \mathcal{K}}{\partial \vec{P}^2}
\tag{63}
$$

and the torus momentum offsets can be calculated from a known frequency offset.

In order to form the new torus with the desired basis frequencies, a new numerical integration must be carried out starting from some new initial conditions, $\vec{X}_0 = \begin{bmatrix} \vec{r}_0^T & \vec{v}_0^T \end{bmatrix}^T$. Therefore, the torus momentum offset must be expressed as a change in physical position and/or velocity. For this effort, the initial position from the TLEs was assumed accurate, and therefore held constant, and the initial velocity was allowed to change.

41

Let the physical and torus state vectors be

$$
\begin{aligned}
\vec{X} &= \begin{bmatrix} \vec{r}^T & \vec{v}^T \end{bmatrix}^T & &= [x\ y\ z\ v_x\ v_y\ v_z]^T \\
\vec{Y} &= \begin{bmatrix} \vec{Q}^T & \vec{P}^T \end{bmatrix}^T & &= [M\ \Omega\ \omega\ P_1\ P_2\ P_3]^T
\end{aligned}
\tag{64}
$$

Then the change in the physical state vector can be written in terms of a change in the torus state vector as

$$
\Delta \vec{X} = \begin{bmatrix} \Delta \vec{r} \\ \Delta \vec{v} \end{bmatrix} = \frac{\partial \vec{X}}{\partial \vec{Y}} \Delta \vec{Y}
\tag{65}
$$

where $\Delta \vec{Y} = \begin{bmatrix} \Delta \vec{Q}^T & \Delta \vec{P}^T \end{bmatrix}^T$. The Jacobian $\frac{\partial \vec{X}}{\partial \vec{Y}}$ can be found analytically as

$$
\frac{\partial \vec{X}}{\partial \vec{Y}} = \left(\frac{\partial \vec{Y}}{\partial \vec{Z}} \frac{\partial \vec{Z}}{\partial \vec{X}} \right)^{-1}
\tag{66}
$$

where

$$
\vec{Z} = [M\ \Omega\ \omega\ a\ e\ i]^T
\tag{67}
$$

is a vector containing the classical orbital elements. For a detailed derivation of the content of $\frac{\partial \vec{X}}{\partial \vec{Y}}$, see [32]. Then, setting the change in initial position, $\Delta \vec{r} = 0$, Equation 65 can be re-written as two linear equations

$$
\Delta \vec{r} = \vec{0} = A \Delta \vec{Q} + B \Delta \vec{P}
\tag{68}
$$

$$
\Delta \vec{v} = C \Delta \vec{Q} + D \Delta \vec{P}
\tag{69}
$$

where A, B, C, and D are quadrants of $\frac{\partial \vec{X}}{\partial \vec{Y}}$:

$$
\frac{\partial \vec{X}}{\partial \vec{Y}} = \begin{bmatrix} A & B \\ C & D \end{bmatrix}
\tag{70}
$$

Given $\Delta \vec{P}$ from Equation 59, the change in initial velocity needed to give a desired change in torus basis frequencies can be found by first solving Equation 68 for $\Delta \vec{Q}$ and then solving Equation 69 for $\Delta \vec{v}$:

$$\Delta \vec{v} = \left(-CA^{-1}B + D \right) \Delta \vec{P} \tag{71}$$

Having now obtained a new initial physical state, $\vec{X}_0$, the torus construction process of Section 3.5 was repeated to find a new torus with updated basis frequencies. These frequencies were again compared to the desired TLE frequencies, and the frequency matching algorithm was repeated until the maximum basis frequency error was down to $\mathcal{O}10^{-12} rad/TU$.

3.7 Physical Coordinate Extraction

The torus with frequencies matching the TLE frequencies was then used to extract physical position and velocity as a function of time. This was done by modifying a Matlab script initially developed by Capt Max Yates to read the torus Fourier series file. The original torus model has coordinates, Q_i, which increment linearly in time at rates equal to the torus basis frequencies

$$Q_i = \omega_i t + Q_{i0} \tag{72}$$

Where the Q_{i0} are the value of each coordinate at epoch. However, as noted in Section 3.2, the TLE data showed that M, Ω, and ω change as quadratic functions of time and, since the initial velocity was allowed to change in the torus fitting process, the Q_{i0} differed slightly from the values calculated in the TLEs. The second-order effects were taken into account in the conversion from torus to physical coordinates by calculating the torus coordinates at each time-step as

$$Q_i = a_{2i}t^2 + \omega_i t + Q_{i0} \tag{73}$$

Where a_{2i} are the 2nd-order coefficients from the TLE curve fits. The change in Q_{i0} was addressed by manually changing the values in the torus file to match the a_{0i} values in the curve fits. Having obtained the torus coordinates, Equation 57 was used to transform to the physical coordinates, $\vec{q} = [X\ Y\ Z]^T$.

3.8 Summary

The procedure for the current work can then be concisely summarized in the following manner:

1. Fit quadratic curves to M, Ω, and ω data from a series of TLEs. Set the desired torus basis frequencies equal to the first-order curve fit coefficients.

2. Numerically integrate the orbit starting from an initial position and velocity derived from the first TLE and SGP4 algorithms.

3. Run the torus construction algorithm to obtain an initial torus with basis frequencies near the desired values from step 1.

4. Perform an iteration of the frequency matching algorithm to match the torus basis frequencies to the desired values.

5. Extract physical torus position data using the torus Fourier series. Calculate the torus coordinates within the Fourier series using the quadratic curve-fits from step 1.

6. Compare the position predicted by the torus to the position at epoch of each TLE.

The results of this procedure for each test object are presented and discussed in the following chapter.

IV. Results

The process described in Chapter III was attempted for each of the four test satellites with varying degrees of success. This chapter will discuss the results from each test case and propose possible causes for the difficulties encountered.

4.1 Delta Rocket Body No. 1 Results

4.1.1 TLE Analysis. The TLE data for M, Ω, and ω can be seen in Figures 11 through 13. The 2nd order curves fit to the data can be seen in Table 5.

The residuals for the Ω and ω data are quite small, on the order of 10^{-4} and 10^{-3} respectively, however the residuals for the mean anomaly are between ± 20 radians. This poor fit is believed to be due to inaccurate revolution number data in the TLE set. This inaccuracy is a result of the way the TLE data is set up. Revolution number is incremented at ascending node crossing, and the TLE epoch time is also set to the time when the satellite is at the ascending node. Having epoch time and revolution number tied to the same point can cause the revolution number to not be incremented properly if the position of the satellite is off slightly from the ascending node. Further analysis could be performed to compensate for these errors, however this analysis was not done as part of the current work.

Because of the poor mean anomaly curve-fit, an attempt was not made to fit a torus to the data for Delta Rocket Body No.1.

Table 5: Delta Rocket Body No. 1 Curve-Fits

Data	a_0 [rad]	a_1 $\left[\frac{rad}{TU}\right]$	a_2 $\left[\frac{rad}{TU^2}\right]$
M	6.6068180759878032	5.36659695481893000	-1.30245451198124E-09
Ω	4.0186766299246193	-3.03925873725682E-4	-4.66094156237480E-13
ω	2.6190404421881577	3.24842080054474E-4	-6.36431896081014E-13

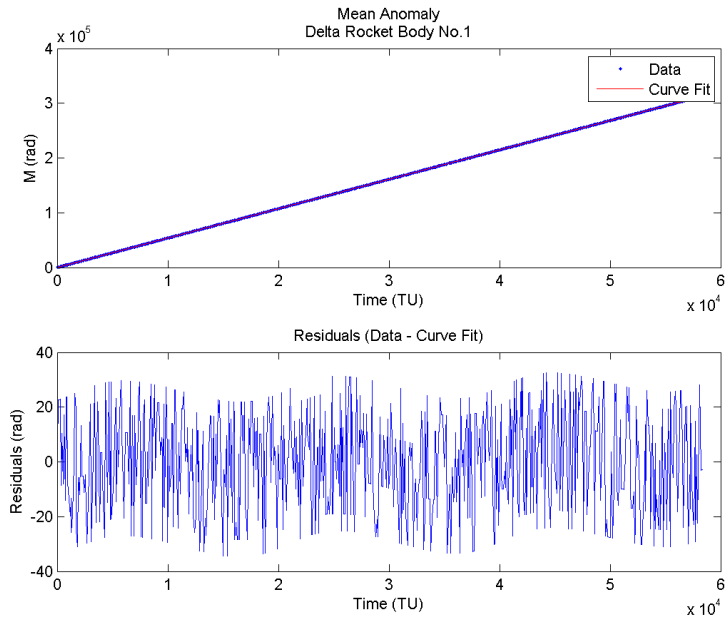*Curve fit of the form: $X = a_0 + a_1 t + a_2 t^2$*

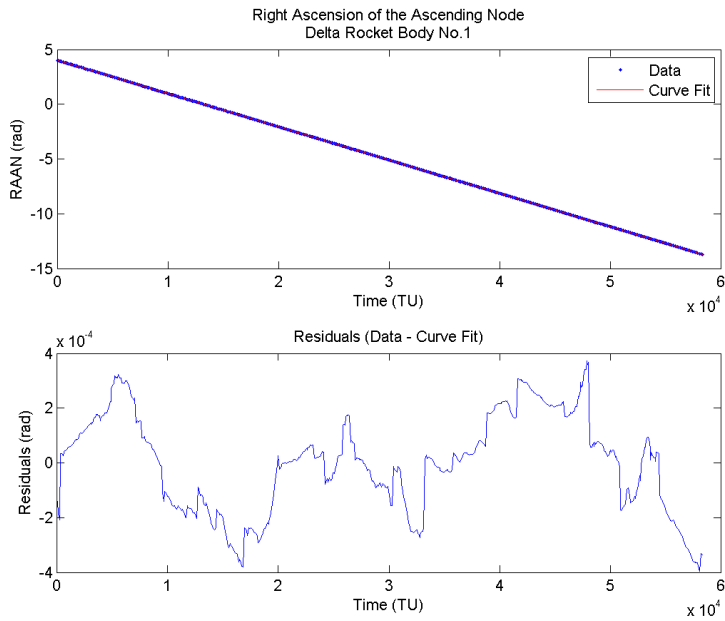Figure 11: Mean Anomaly Data for Delta Rocket Body No.1

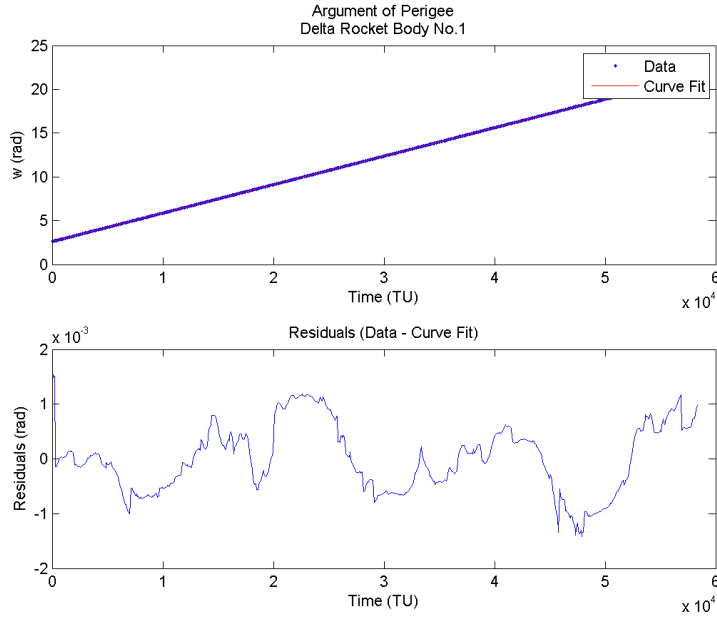Figure 12: RAAN Data for Delta Rocket Body No.1

Figure 13: Argument of Perigee Data for Delta Rocket Body No.1

4.2 Delta Rocket Body No. 2 Results

4.2.1 TLE Analysis. The orbit of Delta Rocket Body No.2 had an eccentricity of approximately 0.03 and had an apogee of only 700km. The TLE data can be seen in Figures 14 through 16. The 2nd order curves fit to the data can be seen in Table 6.

The residuals for the Ω and ω data are again small, although larger than those for Delta Rocket Body No.1, but the mean anomaly residuals are again the largest, this time approximately ± 2 radians. This poor fit could be due to the relatively low altitude of the orbit (perigee at 357km) which would cause this rocket body

Table 6: Delta Rocket Body No. 2 Curve-Fits

Data	a_0 [rad]	$a_1 \left[\frac{rad}{TU}\right]$	$a_2 \left[\frac{rad}{TU^2}\right]$
M	7.46732712440206110	0.88288002293142800	2.28393350843531E-08
Ω	3.68122129498721940	-1.10288004166225E-3	-6.52190507528179E-11
ω	0.17914312485328654	1.88174783746889E-3	1.11759586936959E-10

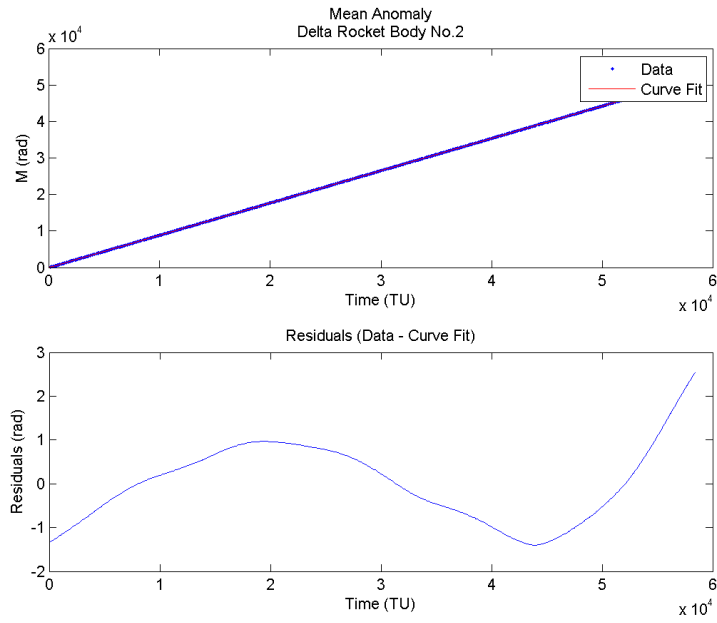*Curve fit of the form: $X = a_0 + a_1 t + a_2 t^2$*

47

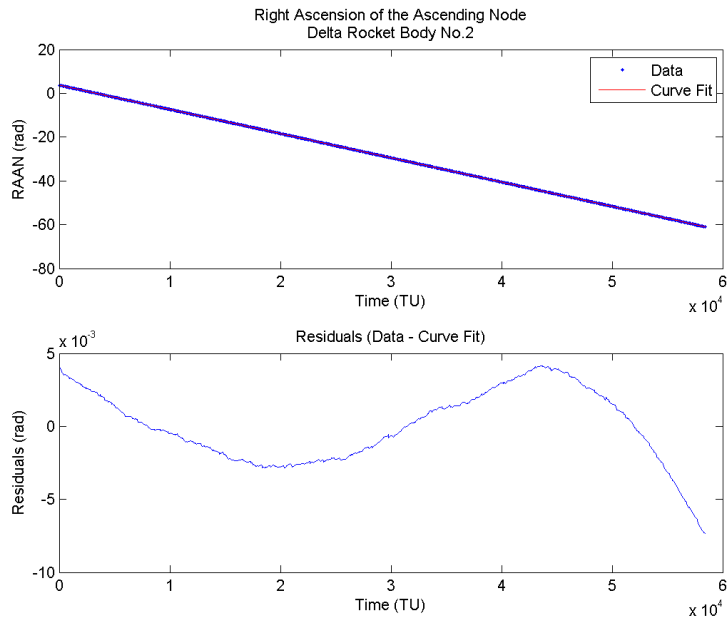Figure 14: Mean Anomaly Data for Delta Rocket Body No.2
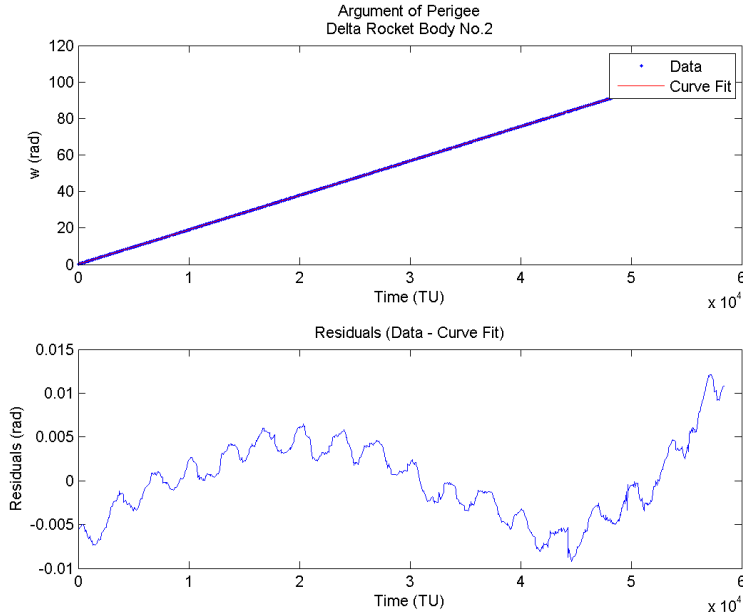

Figure 15: RAAN Data for Delta Rocket Body No.2

Figure 16: Argument of Perigee Data for Delta Rocket Body No.2

to encounter significant air drag. And, while the difference between apogee and perigee is only approximately 350km, because the effect of air drag increases roughly exponentially with decreasing altitude there would still be a significant difference in the amount of air drag felt over the course of an orbit.

Again, because of the poor curve fits, a torus was not fit to the data for Delta Rocket Body No.2.

4.3   Hubble Space Telescope Results

4.3.1   TLE Analysis.   The Hubble Space Telescope is in a nearly circular orbit with eccentricity of approximately 0.0004 at an altitude of approximately 560km. In addition, while the Rocket Bodies analyzed are large hollow cylinders with a large cross-sectional area to mass ratios $\left(\frac{A}{M}\right)$, the HST is filled with optics, cameras, batteries and other equipment which give it much smaller $\frac{A}{M}$. Because of these factors, it was expected the air-drag effects would be less pronounced and nearly uniform

49

throughout the orbit. TLE data can be seen in Figures 17 through 19 while the 2nd order curves fit to the data can be seen in Table 7.

Table 7: Hubble Space Telescope Curve-Fits

Data	a_0 [rad]	$a_1 \left[\frac{rad}{TU}\right]$	$a_2 \left[\frac{rad}{TU^2}\right]$
M	3.48798565697538270	0.88019778693820000	1.01689070044144E-09
Ω	0.71456401402421699	-1.06265838887821E-3	-2.81526562126039E-12
ω	2.71458280469347900	1.73080477457464E-3	-3.66447396216027E-12

Curve fit of the form: $X = a_0 + a_1 t + a_2 t^2$
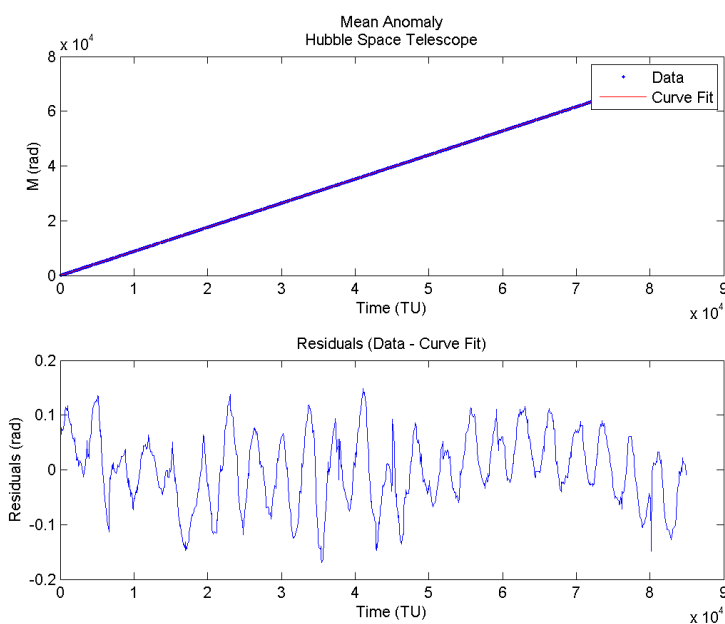

Figure 17: Mean Anomaly Data for the HST

This time, residuals for Ω are still small, but both mean anomaly and ω have residuals of approximately ± 0.1 radian. These residuals may again be influenced by the randomness of air drag caused by changes in the earth's atmosphere. While the residuals may seem small, it is important to remember that an error of 0.1 radians in mean anomaly translates to a position difference of nearly 700km at the HST's orbital altitude. Because of this, a torus accurate to even 10s of kilometers in position would not be possible with the current method, however the torus fitting process was
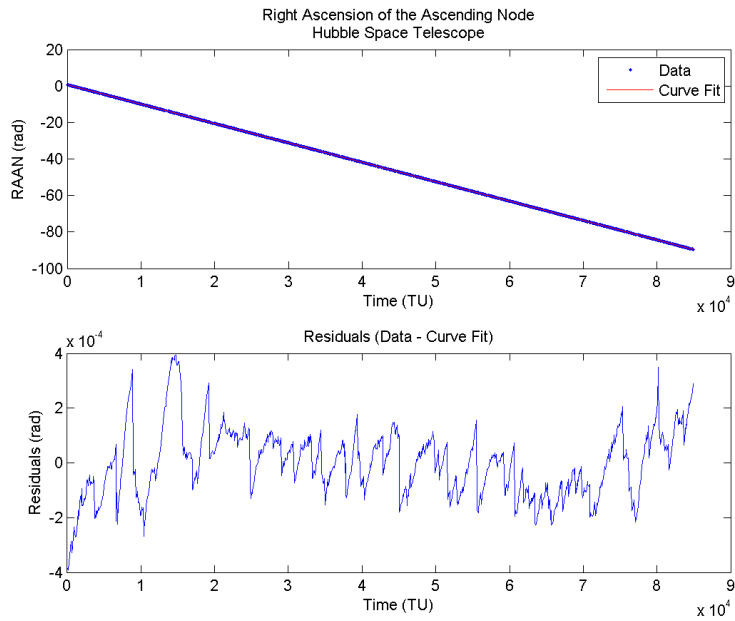
Figure 18: RAAN Data for the HST

still attempted to determine if it would be accurate to expected precision based on the residuals.
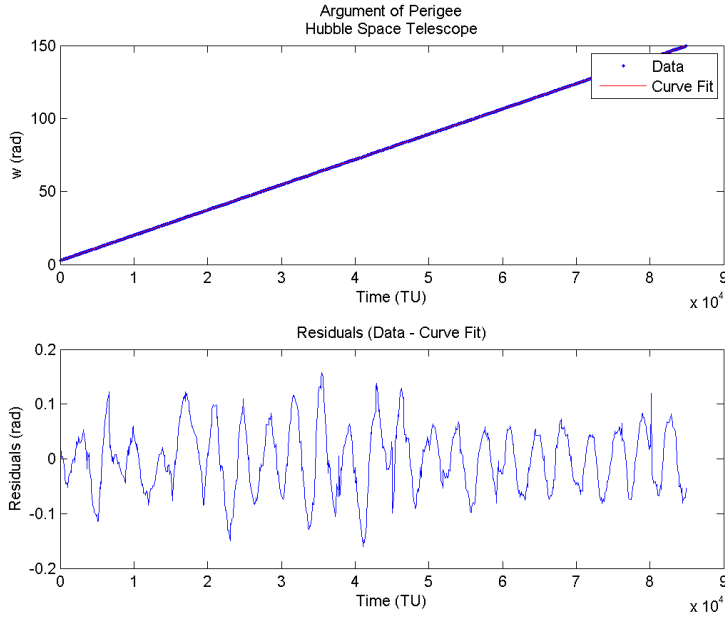
Figure 19: Argument of Perigee Data for the HST

4.3.2 Torus Fitting. The desired frequencies for the HST torus were taken from the first order terms in the curve fits and can be seen in Table 8.

Table 8: Hubble Space Telescope Desired Torus Frequencies

$\omega_1 \left[\frac{rad}{TU}\right]$	$\omega_2 \left[\frac{rad}{TU}\right]$	$\omega_3 \left[\frac{rad}{TU}\right]$
8.801977869382E-1	-5.98963149699971E-2	1.73080477457464E-3

The torus construction process of Section 3.5 was attempted, but failed on the first attempt. The algorithm to identify the basis frequencies in the numerically integrated data failed to correctly identify ω_3 starting from the J_2 estimate. In an attempt to solve this problem, the frequency power spectrum was analyzed manually to get a better estimate of ω_3. Starting from this estimate, the frequency basis set improved, but still had residuals on the order of $10E-5$ which showed that the correct basis frequencies had still not been identified. It is believed that the cause of this difficulty may be the small eccentricity of the HST's orbit. In classical perturbation theory, small eccentricities lead to singularities in the series expansions of the orbital elements. These singularities are dealt with in the SGP4 algorithms by discarding

52

the terms that cause problems [12]. The torus construction method, however, does not neglect these terms and the low eccentricity of the HST's orbit seems to be below the useful tolerance of the current method.

4.4   Thor Rocket Body Results

4.4.1   TLE Analysis.   The Thor Rocket Body is in an orbit with an eccentricity of approximately 0.02 with apogee at an altitude of 1203 km and perigee at 921 km. With this orbit, it was expected that air drag effects would be less pronounced than what was seen with Delta rocket body No.2 or the HST. The TLE data can be seen in Figures 20 through 22 and the curve fits are shown in Table 9.
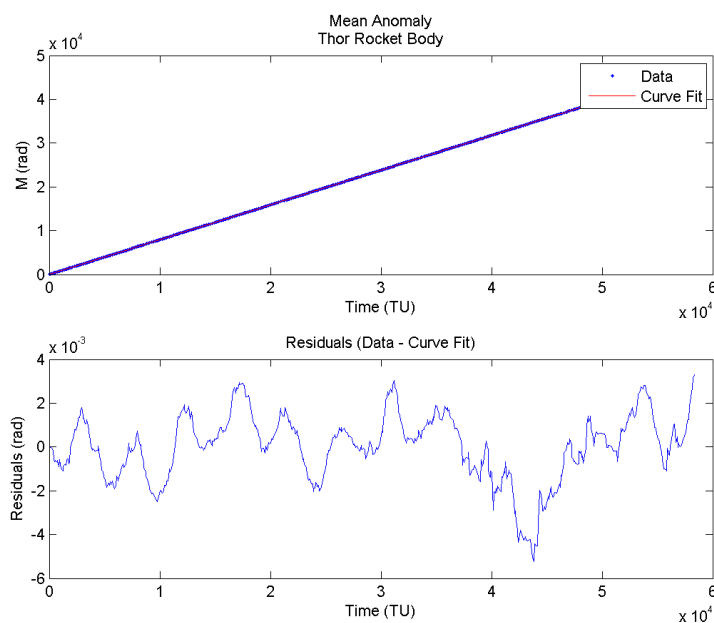

Figure 20: Mean Anomaly Data for the Thor Rocket Body

This time, all residuals were small with a maximum value of approximately $5E-3$ seen in the mean anomaly residuals. Because of this, the torus fitting process was attempted.
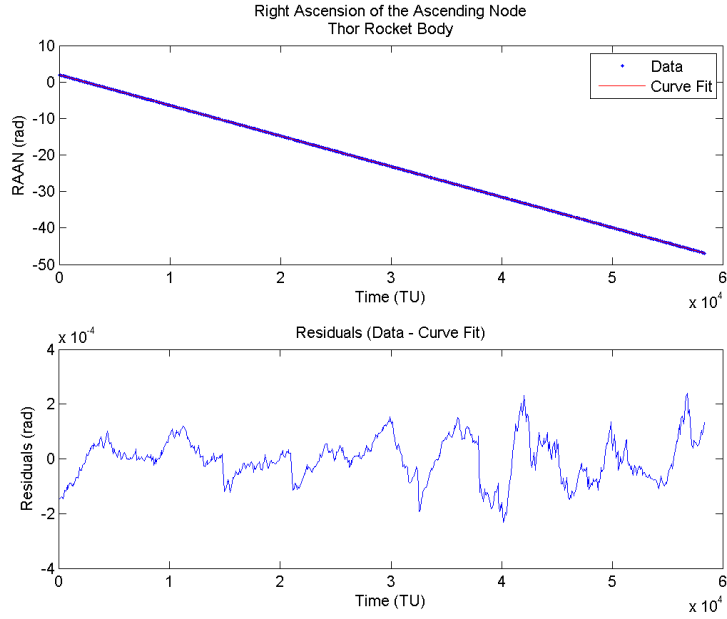
Figure 21: RAAN Data for the Thor Rocket Body

Table 9: Thor Rocket Body Curve-Fits

Data	$\mathbf{a_0}$ [rad]	$\mathbf{a_1}$ $\left[\frac{\mathbf{rad}}{\mathbf{TU}}\right]$	$\mathbf{a_2}$ $\left[\frac{\mathbf{rad}}{\mathbf{TU^2}}\right]$
M	4.8169895251603805	0.79372722076537100	5.93349302063384E-11
Ω	1.9555018406270159	-8.36935587639413E-4	-1.45394333352382E-13
ω	1.5043570873484007	1.36750321345161E-3	4.85354594310724E-13

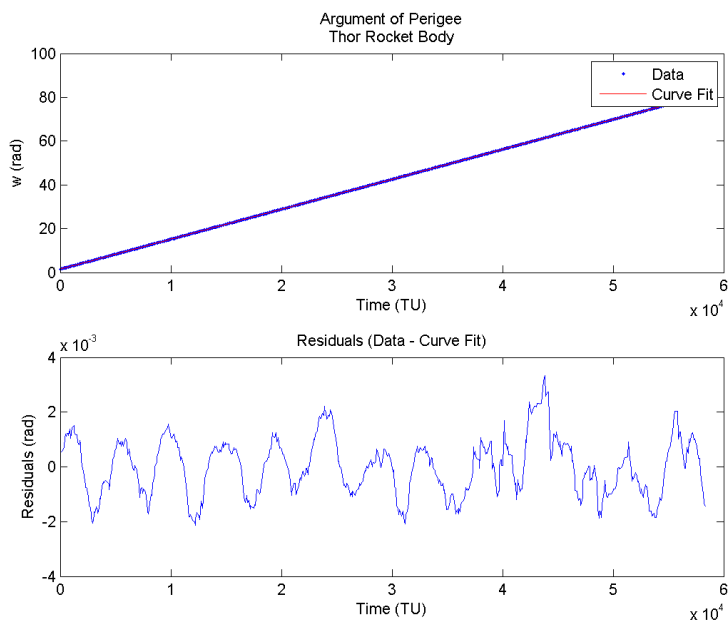Curve fit of the form: $X = a_0 + a_1 t + a_2 t^2$

54

Figure 22: Argument of Perigee Data for the Thor Rocket Body

4.4.2 Torus Fitting. Based on the curve fits, the desired torus basis frequencies were determined and are shown in Table 10. Starting from the initial po-

Table 10: Thor Rocket Body Desired Torus Frequencies

$\omega_1 \left[\frac{rad}{TU}\right]$	$\omega_2 \left[\frac{rad}{TU}\right]$	$\omega_3 \left[\frac{rad}{TU}\right]$
7.9372722076537E-1	-5.96705921687582E-2	1.3675032134516E-3

sition and velocity determined using the SGP4 code and the first TLE, the process of creating a torus and matching the basis frequencies to the desired set described in Sections 3.5 and 3.6 was accomplished. A total of four iterations of the frequency matching algorithm were necessary to match the torus basis frequencies to within the desired tolerance. Table 11 shows the progression of torus frequencies and Table 12 shows the initial velocity changes made at each iteration of the frequency matching process.

Table 11: Torus Frequency Matching for Thor Rocket Body

	$\omega_1 \left[\frac{rad}{TU}\right]$	$\omega_2 \left[\frac{rad}{TU}\right]$	$\omega_3 \left[\frac{rad}{TU}\right]$
Initial Torus	7.93732038441640E-01	-5.96704909422124E-02	1.36749993586527E-03
Iteration 1 Torus	7.93718780146312E-01	-5.96705786750190E-02	1.36747666904746E-03
Iteration 2 Torus	7.93727192361304E-01	-5.96705924650170E-02	1.36750386446849E-03
Iteration 3 Torus	7.93727221037809E-01	-5.96705921734135E-02	1.36750322508483E-03
Iteration 4 Torus	7.93727220771728E-01	-5.96705921687751E-02	1.36750321348700E-03
	ω_1 residual $\left[\frac{rad}{TU}\right]$	ω_2 residual $\left[\frac{rad}{TU}\right]$	ω_3 residual $\left[\frac{rad}{TU}\right]$
Iteration 1 Torus	8.44061905791449E-06	-1.34937392023970E-08	2.65444041400165E-08
Iteration 2 Torus	2.84040659881413E-08	2.96258795273729E-10	-6.51016889919101E-10
Iteration 3 Torus	-2.72439071302699E-10	4.65529698123746E-12	-1.16332299696098E-11
Iteration 4 Torus	-6.35802521742335E-12	1.68962066560141E-14	-3.53998514529552E-14

Table 12: Changes to Initial Velocity in Thor Rocket Body Torus Fitting Process

	$V_x \left[\frac{DU}{TU}\right]$	$V_y \left[\frac{DU}{TU}\right]$	$V_z \left[\frac{DU}{TU}\right]$
Initial Velocity	-9.98015949328921E-2	-8.11259141324669E-1	4.39329318458694E-1
Iteration 1 ΔV	2.45940386540720E-3	-2.58556420032001E-4	8.51464239486448E-5
Iteration 2 ΔV	-1.09486652807646E-4	1.50534148714208E-5	-3.35944758461485E-6
Iteration 3 ΔV	-3.85930049076970E-6	5.54734206659374E-7	1.45063141307529E-7
Iteration 4 ΔV	-3.20433729724457E-8	5.37472590607683E-9	3.03779212051191E-9
Total ΔV	-2.34602586873582E-3	2.42942896228060E-4	-8.19350772974792E-5

The magnitude of the total velocity change was approximately 0.25 percent of the initial velocity magnitude obtained from the TLEs and SGP4. This corresponds to approximately 19 m/s and is well within the uncertainty in velocity predictions using SGP4.

4.4.3 Position Comparison.   After a torus was formed with the desired basis frequency set, the torus coordinates were transformed to physical coordinates using Equation 57 and a Matlab script. This physical position was then compared to the numerically integrated position to determine if the torus matched the data it was fit to. The results of this comparison can be seen in Figure 23.
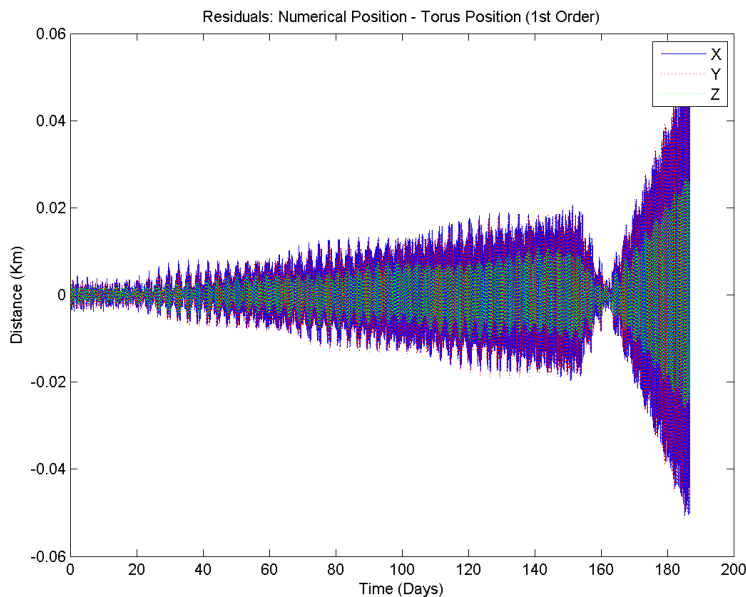

Figure 23: Comparison of Numerically Integrated Position to Torus Position, 1st order Q_i

The torus position matches the numerically integrated position to within approximately 60 meters in any of the three axes over 6 months. The abrupt change in the error growth rate seen at approximately 170 days is the result of the torus coordinate calculations reaching the limit of double precision accuracy.

The position predicted by the torus was then calculated at each TLE epoch time and compared to the SGP4 position. This was initially done using only the first order curve-fit terms (the basis frequencies) to update the torus coordinates, Q_i, and the initial torus coordinate values, Q_{i0}, calculated in the torus construction process. The results of this comparison can be seen in Figures 24 and 25.
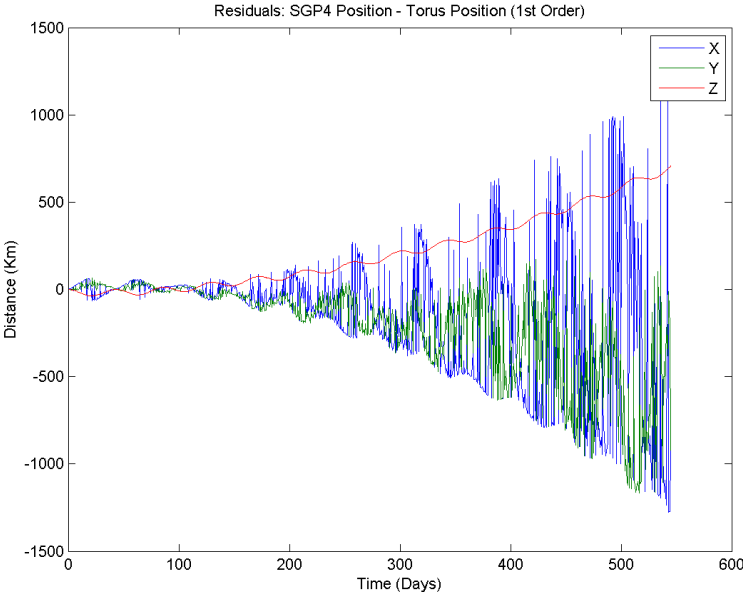

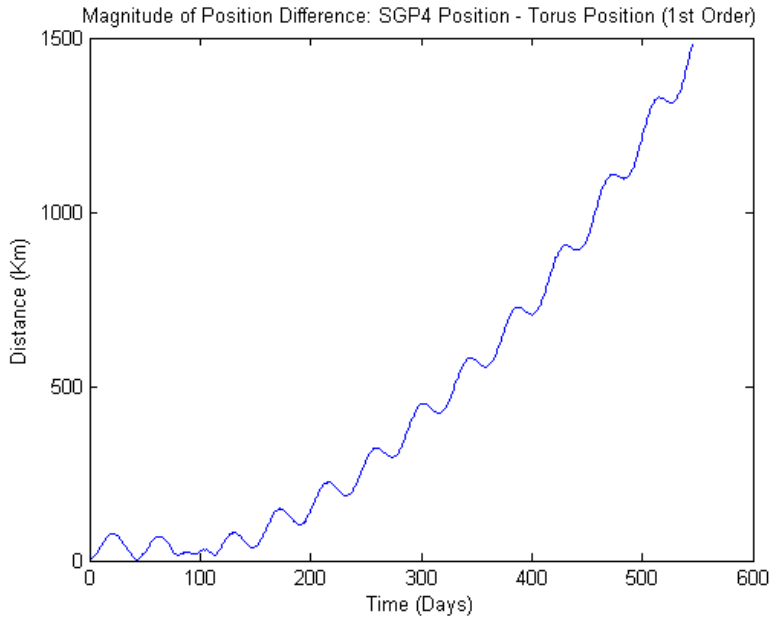Figure 24: Residuals: SGP4 Position - Torus Position, 1st order Q_i

Figure 25: Error Magnitude: SGP4 Position - Torus Position, 1st order Q_i

It is evident that the torus in this configuration provides a poor position prediction with the error in position going to nearly 1500km after 18 months. This, however, is expected as the TLE analysis showed that the torus coordinates, M, Ω, and ω increase as quadratic, 2nd order functions of time, not first order. To compensate for this, the 2nd order curve-fit coefficients were included in the calculation of the $Q_i's$ at each time-step and the torus position was again compared to the SGP4 position. The results of this comparison can be seen in Figures 26 and 27.
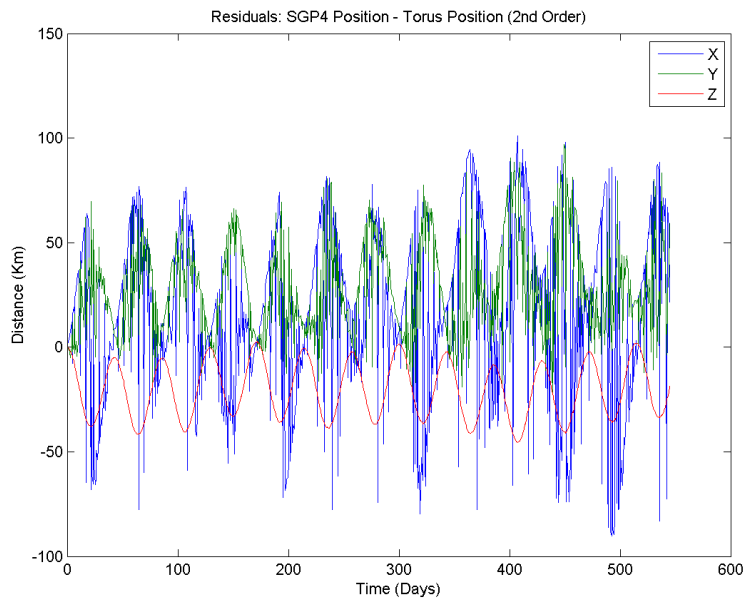
Figure 26: Residuals: SGP4 Position - Torus Position, 2nd order Q_i

Figure 27: Error Magnitude: SGP4 Position - Torus Position, 2nd order Q_i

These plots show that adding the 2nd order terms to the torus coordinates drastically improve the torus position predictions, with the maximum error now being approximately 110km, or less than 10 percent of the previous error. It is also important to note that the linear portion of the error growth has been nearly eliminated leaving only periodic oscillations.

In an effort to further refine the torus position prediction, the a_0 terms for the curve-fits were used to replace the Q_{i0} values calculated in the torus construction process. This replacement is shown in Equation 74.

$$Q_{10} = M_0$$
$$Q_{20} = \Omega_0 - GMST_0 \tag{74}$$
$$Q_{30} = \omega_0$$

The torus position was again compared to the SGP4 position and can be seen in Figures 28 and 29.
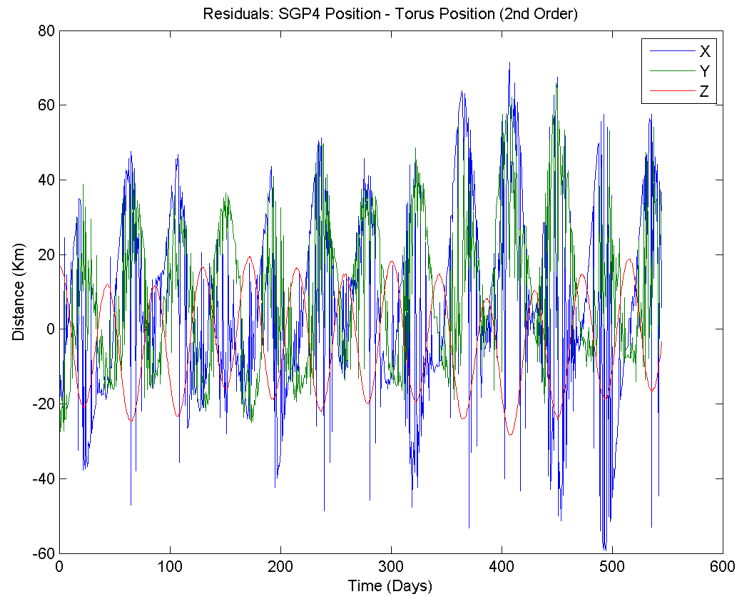

Figure 28: Residuals: SGP4 Position - Torus Position, 2nd order Q_i, Q_{0i} from curve fits
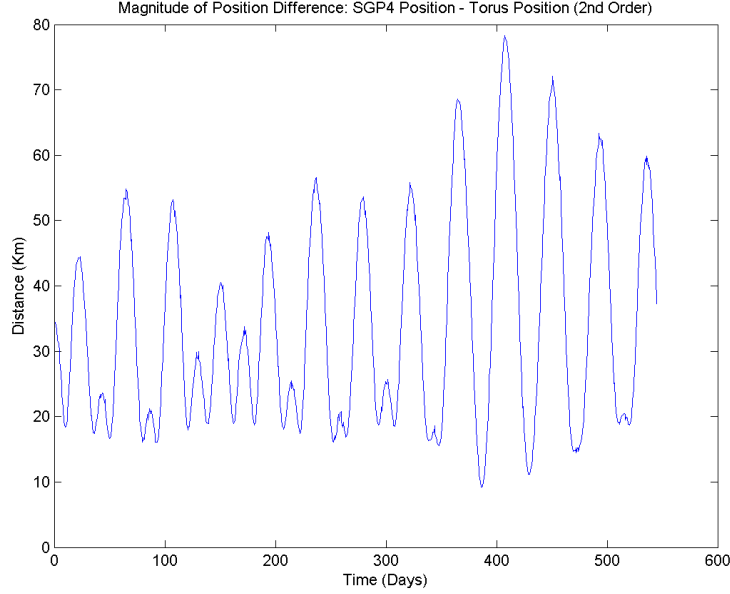
Figure 29: Error Magnitude: SGP4 Position - Torus Position, 2nd order Q_i, Q_{0i} from curve fits

This comparison shows a number of notable results. First, the maximum error is now down to approximately 78km; a 29 percent reduction from the error obtained using the initial Q_{i0} values. Second, there is now error present at t=0. This initial error is due to the fact that the values of the curve fits for M, Ω, and ω at t=0 are not exactly equal to the values in the first TLE. Finally, the amplitude of oscillation in the X, Y, and Z error has decreased. This is shown in Table 13.

Table 13: Comparison of Position Error Oscillation Amplitude

	X Error Oscillation Amplitude [km]	Y Error Oscillation Amplitude [km]	Z Error Oscillation Amplitude [km]
Initial Q_{i0}	155 - 180	85 - 120	35 - 42
Curve fit Q_{i0}	85 - 125	55 - 86	37 - 39

While this representation of the torus does drastically reduce the error in position from the initial torus with first-order Q's, it still does not provide anywhere near the accuracy that would be required for operational use. In an effort to determine the cause of the error, the periodic nature of the error was examined.

62

Figure 28 shows that the X and Y error oscillations are nearly in-phase, while the Z oscillations are offset by 180 degrees. It is also interesting to note that the Z error oscillations seem to have only one frequency, while the X and Y oscillations have at least two distinct frequencies. The period between peaks in the Z data is approximately 42.2 to 43.3 days, which is also the period between the major peaks in the X and Y data. This period corresponds to the period of ω_3, which is 42.905 days. To further verify this, a FFT was performed on the position error data to analyze its frequency content. Figure 30 shows the frequency power spectrum over the entire range of frequencies studied.
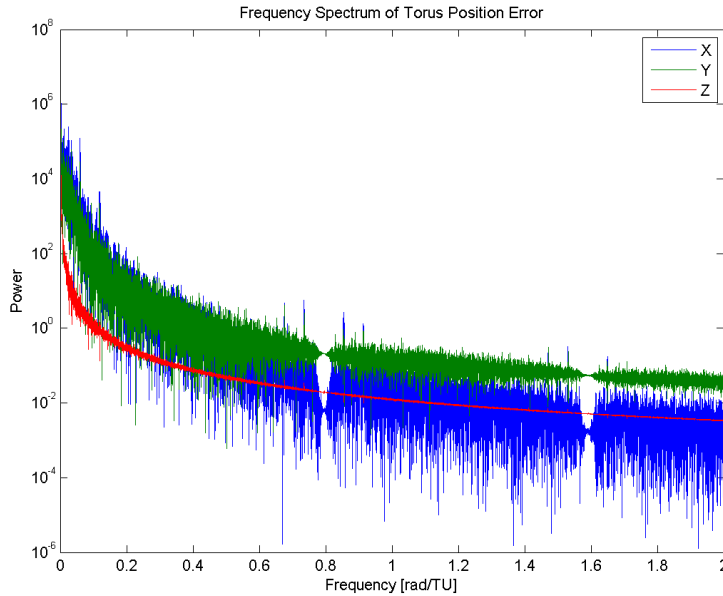

Figure 30: Frequency Power Spectrum for Torus Position Error

The spectrum is quite noisy, but clearly has maximum power in the smaller frequencies. The two points in the spectrum where the oscillations appear to temporarily damp out are centered around frequencies equal to the torus' ω_1 and $2\omega_1$. Figure 31 shows detail around ω_1. It is clear that there is no peak at ω_1, but there are small peak clusters at intervals of $\pm\omega_2$ separated by ω_3 in the X and Y spectra. Figure 32 shows detail around the torus' ω_3 value and shows that, as expected, all

three coordinates have maximum power at this frequency. Also, as expected, the Z coordinate power spectrum drops off sharply around the ω_3 value while the X and Y spectra have other maxima of similar magnitude nearby.
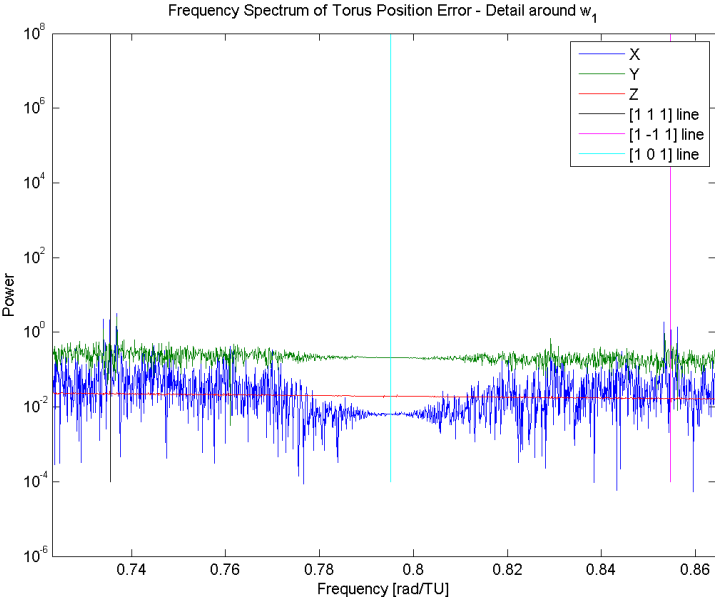

Figure 31: Frequency Power Spectrum for Torus Position Error - ω_1 detail
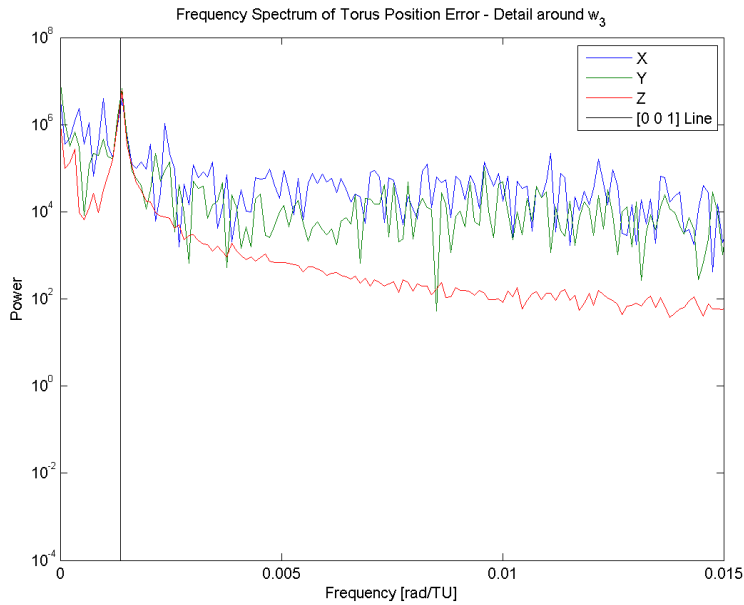
Figure 32: Frequency Power Spectrum for Torus Position Error - ω_3 detail

Figure 33 shows detail around the torus' ω_2 value and clearly shows three more peaks in X and Y at positions corresponding to ω_2 and $\omega_2 \pm \omega_3$. The Z coordinate is not expected to have peaks at these locations because ω_2, or $\dot{\Omega}$, has minimal impact on Z-position. (Recall that the numerically integrated Z-Coordinate data did not have peaks at [1 1 1] or [1 -1 1]).
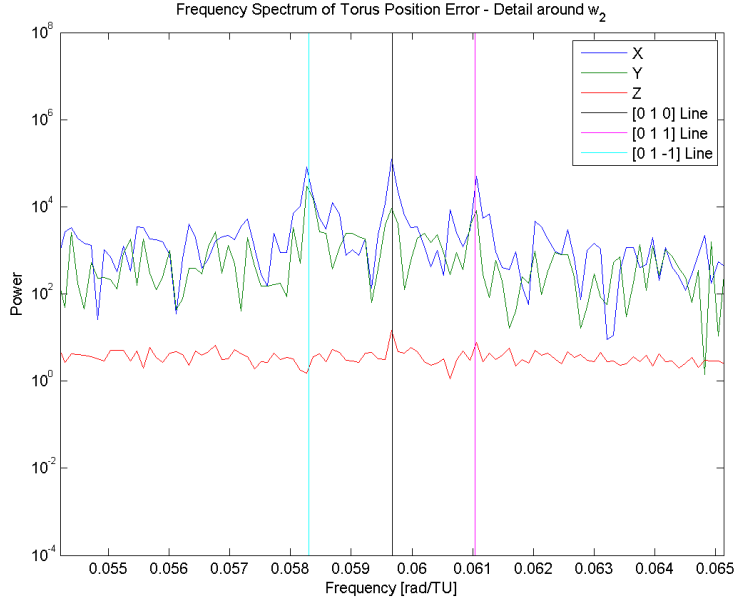
Figure 33: Frequency Power Spectrum for Torus Position Error - ω_2 detail

This analysis suggests that the torus construction algorithm does not adequately characterize the impacts of ω_3 and, to a smaller extent, ω_2 on the satellite's position. In order to determine if this deficiency was caused by too few terms in the Fourier series, another torus was constructed containing additional ω_3 terms, however the position error measured against the TLE and SGP4 data was unchanged. Because of this, it is believed that the algorithm used to calculate the Fourier series coefficients through simultaneously analyzing clusters of peaks is not working properly. In this method, clusters of peaks are studied in order of decreasing magnitude. Each peak cluster is analyzed in order to determine its Fourier coefficients and subsequently removed from the data. This technique is used in the hope that removing larger peak clusters will allow more precise analysis of smaller clusters which would otherwise be obscured by their larger neighbors. The holes in the power spectrum of the position error at ω_1 and $2\omega_1$ demonstrate that the larger ω_1 peak clusters have been successfully eliminated, however the appearance of peaks surrounding ω_2 and ω_3 suggest that these smaller peak clusters have not been removed properly from

66

the data. In his research, Bordner also experienced problems in properly characterizing the impact of ω_3 [2]. He concluded that these problems stemmed from two sources. First, that if the orbital data analyzed spanned too short a time period then the effect of ω_3 could not be captured due to it's long period, and second that low eccentricity orbits would also encounter difficulty due to small divisors. It was believed that the current work would avoid each of these issues as the time period of data used to construct the torus is approximately 13 times the period of ω_3 and the eccentricity of the orbit is approximately 0.02. Further research is needed to verify that the current difficulty is another manifestation of problems faced by Bordner, or if it is a new issue entirely.

V. Conclusions

Chapter IV shows a number of promising results. First, the HST and Thor Rocket Body test cases show that it is possible to extract accurate KAM torus basis frequencies from observational data in the form of TLEs. Second, a method of making slight changes to torus basis frequencies was demonstrated by equating a desired change in basis frequencies to a small change in initial velocity. This capability allows the current torus construction method to be used in tandem with the TLE frequency identification routine to obtain a torus with the desired basis frequencies for a given satellite.

The difficulties encountered with TLE curve fitting for the two Delta Rocket Bodies show that there may be a only a limited subset of orbital regimes for which basis frequency extraction from TLEs can be useful; Specifically, orbital regimes with moderate inclination and eccentricity where air drag is minimal and nearly constant throughout the orbit. The difficulty seen in the torus construction process for the HST and the poor characterization of ω_2 and ω_3 in the Thor Rocket Body test case reinforces the fact that small eccentricity orbits cannot be modeled to the desired degree of accuracy with the current KAM torus construction method.

5.1   Recommendations for Further Study

First, an investigation into the failure of the peak-cluster decomposition method of calculating Fourier Coefficients seen in the Thor Rocket Body test case is needed. This test case should be continued, either using an updated peak-cluster method or using the original Laskar method of analyzing each peak individually. This investigation should be completed to show the true accuracy of the torus model.

Next, a broader survey is needed of satellites in a variety of orbits. This analysis should be conducted to show the limits of eccentricity, inclination, and orbital period that form the boundaries of the 'orbital box' in which the extraction of torus basis frequencies from TLEs is possible. Another study could be done to determine the

time period of TLE data that is necessary to obtain accurate basis frequencies. It would also be beneficial to investigate the possibility of reformulating the current torus construction method in Poincare elements. If successful, this could eliminate the problems currently faced in applying the KAM torus model to earth satellites in low eccentricity orbits.

This research on the contribution of TLE data to KAM torus construction should also be incorporated with the research currently being done by Capt's Hagen and Yates. Their projects will add air drag and the effect of the moon to the torus model as well as a method of moving between nearby tori with slightly different momenta. This integration could increase the accuracy of torus position prediction and possibly allow the construction of accurate tori for satellites with larger residuals in their TLE curve-fits due to their orbits or periodic station-keeping maneuvers. A study could also be conducted to determine how much of the residuals seen in the TLE curve-fits are due to stochastics, such as variation in air-drag, and how much is due to other perturbations that have not, or cannot, be modeled easily.

Finally, an analysis should be conducted to compare the accuracy of a KAM torus to the SGP4 propagation algorithms. This analysis could show the possible benefits of using a KAM torus model in place of the current SGP4 model in predicting future satellite positions.

Bibliography

1. Arnol'd, V.I. "Proof of a Theorem of A.N. Kolmogorov on the Invariance of Quasi-Periodic Motions Under Small Perturbations of the Hamiltonian," *Russian Mathematical Surveys*, *18*(5):9–36 (1963).

2. Bordner, Ralph E. *Orbital Tori Construction Using Trajectory Following Spectral Methods*. PhD dissertation, Air Force Institute of Technology, 2010.

3. Brouwer, Dirk. "Solution of the Problem of Artificial Satellite Theory Without Drag," *Astronomical Journal*, *64*(1274):378–397 (1959).

4. Celletti, Alessandra. "Some KAM Applications to Celestial Mechanics," *Discrete and Continuous Dynamical Systems Series S*, *3*(4):533–544 (2010).

5. Celletti, Alessandra and Luigi Chierchia. "KAM Stability for a Three-Body Problem of the Solar System," *Zeitschrift Fur Angewandte Mathematik Und Physik*, *57*(1):33–41 (2006).

6. "Chinese ASAT Test," August 2010. 17 October 2010 http://www.celestrak.com/events/asat.asp.

7. Craft, Christopher T. *Formation Flight of Earth Satellites on KAM Tori*. MS thesis, Air Force Institute of Technology, 2009.

8. Danby, J.M.A. *Fundamentals of Celestial Mechanics* (Second Edition). Willmann-Bell, Inc., 1998.

9. Derbis, Rachael M. *Modeling GPS Satellite Orbits Using KAM Tori*. MS thesis, Air Force Institute of Technology, 2008.

10. "EGM96: The NASA GSFC and NIMA Joint Geopotential Model." 12 December 2010, http://cddis.gsfc.nasa.gov/926/egm96/egm96.html.

11. Goldstein, Herbert and others. *Classical Mechanics* (Third Edition). Addison Wesley, 2002.

12. Hoots, Felix R., et al. "History of Analytical Orbit Modeling in the U.S. Space Surveillance System," *Journal of Guidance, Control, and Dynamics*, *27*(2):174–185 (2004).

13. "Iridium 33/Cosmos 2251 Collision," September 2010. 17 October 2010 http://www.celestrak.com/events/collision/.

14. Kelso, Dr. T.S., "Orbit Determination," July/August 1995. 8 December 2010 http://celestrak.com/columns/v01n06/.

15. Kelso, T.S. "Validation of SGP4 and IS-GPS-200D Against GPS Precision Ephemerides." *17th AAS/AIAA Space Flight Mechanics ConferenceAAS 07-127*. 28 January-1 February 2007.

16. Kessler, Donald J. "Collisional Cascading: The Limits of Population Growth in Low Earth Orbit," *Advances in Space Research*, *11*(12):(12)63–(12)66 (1991).

17. Kozai, Yoshihide. "The Motion of a Close Earth Satellite," *Astronomical Journal*, *64*(1274):367–377 (1959).

18. Lane, Max H. and K.H. Cranford, "An Improved Analytical Drag Theory for the Artificial Satellite Problem." AIAA Paper, 1969.

19. Laskar, J. *Introduction to Frequency Map Analysis*, 134–150. NATO ASI Series, Series C: Mathematical and Physical Sciences - Vol.53, 1999. Edited by C. Simo.

20. Little, Bryan, D. *Application of KAM Theorem to Earth Orbiting Satellites*. MS thesis, Air Force Institute of Technology, 2009.

21. Lyddane, R.H. "Small Eccentricities or Inclinations in the Brouwer Theory for the Artificial Satellite Problem," *Astronomical Journal*, *68*(8):555–558 (1963).

22. McGill, Colin and James Binney. "Torus Construction in General Gravitational Potentials," *Monthly Notices Royal Astronomical Society*, *244*:634–645 (1990).

23. NASA. "Space Missions and Orbital Box Score," *Orbital Debris Quarterly News*, *14*(1):12 (2010).

24. NASA. "Top Ten Satellite Breakups," *Orbital Debris Quarterly News*, *14*(3):2 (2010).

25. Poschel, J. "A Lecture on the Classical KAM Theorem." *Symposia in Pure Mathematics (AMS)69, 707-732*. 2009.

26. Robutel, Philippe. "An Application of KAM Theory to the Planetary Three Body Problem," *Celestrial Mechanics and Dynamical Astronomy*, *56*(1-2):197–199 (1993).

27. "Space Surveillance." 10 October 2010 http://www.au.af.mil/au/awc/awcgate/usspc-fs/space.htm.

28. "USSTRATCOM Space Control and Space Surveillance Factsheet," February 2008. 1 October 2010 http://www.stratcom/mil/files/STRATCOM_Space_and_Control_fact_Sheet-25_Feb_08.doc.

29. Vallado, David A., "Computer Software in MATLAB." 5 December 2010, http://celestrak.com/software/vallado-sw.asp.

30. Vallado, David A. *Fundamentals of Astrodynamics and Applications* (Third Edition). Microcosm Press, 2007.

31. Wayne, C. Eugene, "An Introduction to KAM Theory," 22 January 2008. 26 October 2010 http://math.bu.edu/people/cew/preprints/introkam.pdf.

32. Wiesel, William E. "Motion Near an Earth Satellite KAM Torus." Unpublished Working Document.

33. Wiesel, William E. "Earth Satellite Orbits as KAM Tori," *The Journal of the Astronautical Sciences*, *56*(2):151–162 (2008).

34. Wiesel, William E. "Earth Satellite Perturbation Theories as Approximate KAM Tori," *American Astronomical Society*, *10*(122) (2010).

35. Wiesel, William E. *Modern Astrodynamics* (Second Edition). Aphelion Press, 2010.

36. Wiesel, William E. *Modern Orbit Determination* (Second Edition). Aphelion Press, 2010.

REPORT DOCUMENTATION PAGE

Form Approved
OMB No. 0704–0188

1. REPORT DATE (DD–MM–YYYY)	2. REPORT TYPE	3. DATES COVERED (From — To)
24 03 2011	Master's Thesis	14 Aug 2009 – 24 Mar 2011

4. TITLE AND SUBTITLE	5a. CONTRACT NUMBER
KAM Torus Frequency Generation from Two-Line Element Sets	5b. GRANT NUMBER
	5c. PROGRAM ELEMENT NUMBER
6. AUTHOR(S)	5d. PROJECT NUMBER
Gregory R. Frey, Capt, USAF	5e. TASK NUMBER
	5f. WORK UNIT NUMBER

7. PERFORMING ORGANIZATION NAME(S) AND ADDRESS(ES)	8. PERFORMING ORGANIZATION REPORT NUMBER
Air Force Institute of Technology Graduate School of Engineering and Management (AFIT/ENY) 2950 Hobson Way WPAFB OH 45433-7765	AFIT/GA/ENY/11-M04

9. SPONSORING / MONITORING AGENCY NAME(S) AND ADDRESS(ES)	10. SPONSOR/MONITOR'S ACRONYM(S)
Intentionally Left Blank	11. SPONSOR/MONITOR'S REPORT NUMBER(S)

12. DISTRIBUTION / AVAILABILITY STATEMENT
APPROVED FOR PUBLIC RELEASE; DISTRIBUTION UNLIMITED

13. SUPPLEMENTARY NOTES
This material is declared a work of the U.S. Government and is not subject to copyright protection in the United States.

14. ABSTRACT

The Kolmogorov Arnold and Moser (KAM) theorem states that a lightly perturbed Hamiltonian system will have solutions which lie on a torus. The trajectories of Earth orbiting satellites have been shown to lie on KAM tori with three basis frequencies. These basis frequencies are determined by fitting second order polynomials to data from Two-Line Element sets (TLEs) using a least squares technique. The first order coefficients are used as the torus basis frequencies while the second order coefficients are used to account for perturbations to the satellite's orbit such as air drag. Four cases are attempted using the Hubble Space Telescope and three rocket bodies as test subjects. A KAM torus with the desired basis frequencies is constructed and used to predict satellite position. This position prediction is compared to the position obtained from TLEs using Simplified General Perturbations 4 (SGP4) algorithms. Analysis of the torus position error shows that the torus construction algorithm does not fully characterize the contribution of the smaller basis frequencies to the orbital trajectory.

15. SUBJECT TERMS
KAM, Torus, Two-Line Element Set, Satellite, Orbital Mechanics

16. SECURITY CLASSIFICATION OF:			17. LIMITATION OF ABSTRACT	18. NUMBER OF PAGES	19a. NAME OF RESPONSIBLE PERSON
					William E. Wiesel, PhD; Instructor, AFIT
a. REPORT	b. ABSTRACT	c. THIS PAGE	UU	84	19b. TELEPHONE NUMBER (Include Area Code) (937)255-3636, ext 4312 Email: William.wiesel@afit.edu
U	U	U			

Standard Form 298 (Rev. 8–98)
Prescribed by ANSI Std. Z39.18